



LoVoCCS. II. Weak Lensing Mass Distributions, Red-sequence Galaxy Distributions, and Their Alignment with the Brightest Cluster Galaxy in 58 Nearby X-Ray-luminous Galaxy Clusters

Shenming Fu¹ , Ian Dell'Antonio² , Zacharias Escalante² , Jessica Nelson² , Anthony Englert² , Søren Helhoski² , Rahul Shinde² , Julia Brockland², Philip LaDuka², Christelyn Larkin² , Lucca Paris², Shane Weiner², William K. Black³ , Ranga-Ram Chary⁴ , Douglas Clowe⁵ , M. C. Cooper⁶ , Megan Donahue⁷ , August Evrard^{8,9} , Mark Lacy¹⁰ , Tod Lauer¹ , Binyang Liu¹¹ , Jacqueline McCleary¹² , Massimo Meneghetti^{13,14} , Hironao Miyatake^{15,16,17} , Mireia Montes^{18,19} , Priyamvada Natarajan^{20,21} , Michelle Ntampaka^{22,23} , Elena Pierpaoli²⁴ , Marc Postman²⁵ , Jubee Sohn^{26,27} , David Turner⁷ , Keiichi Umetsu²⁸ , Yousuke Utsumi²⁹ , and Gillian Wilson³⁰

¹ NSF's National Optical-Infrared Astronomy Research Laboratory, 950 North Cherry Avenue, Tucson, AZ 85719, USA; shenming.fu.astro@gmail.com

² Department of Physics, Brown University, 182 Hope Street, Box 1843, Providence, RI 02912, USA

³ Department of Physics and Astronomy, Brigham Young University, N283 ESC, Provo, UT 84602, USA

⁴ Infrared Processing and Analysis Center, MC 314-6, Caltech, 1200 E. California Boulevard, Pasadena, CA 91125, USA

⁵ Department of Physics and Astronomy, Ohio University, 1 Ohio University, Athens, OH 45701, USA

⁶ Department of Physics and Astronomy, University of California, Irvine, Irvine CA, USA

⁷ Department of Physics and Astronomy, Michigan State University, East Lansing, MI 48824, USA

⁸ Department of Astronomy, University of Michigan, Ann Arbor, MI 48109, USA

⁹ Department of Physics, University of Michigan, Ann Arbor, MI 48109, USA

¹⁰ National Radio Astronomy Observatory, 520 Edgemont Road, Charlottesville, VA 22903, USA

¹¹ Purple Mountain Observatory, Chinese Academy of Sciences, Nanjing 210023, People's Republic of China

¹² Department of Physics, Northeastern University, 110 Forsyth Street, Boston, MA 02115, USA

¹³ Osservatorio di Astrofisica e Scienza dello Spazio di Bologna, Istituto Nazionale di Astrofisica, Via Gobetti 93/3, I-40129, Bologna, Italy

¹⁴ National Institute for Nuclear Physics, viale Berti Pichat 6/2, I-40127 Bologna, Italy

¹⁵ Kobayashi-Maskawa Institute for the Origin of Particles and the Universe (KMI), Nagoya University, Nagoya, 464-8602, Japan

¹⁶ Division of Physics and Astrophysical Science, Graduate School of Science, Nagoya University, Nagoya 464-8602, Japan

¹⁷ Kavli Institute for the Physics and Mathematics of the Universe (WPI), The University of Tokyo Institutes for Advanced Study (UTIAS), The University of Tokyo, Chiba 277-8583, Japan

¹⁸ Instituto de Astrofísica de Canarias, c/ Vía Láctea s/n, E-38205 - La Laguna, Tenerife, Spain

¹⁹ Departamento de Astrofísica, Universidad de La Laguna, E-38205 - La Laguna, Tenerife, Spain

²⁰ Department of Astronomy, Yale University, 266 Whitney Avenue, New Haven, CT 06511, USA

²¹ Department of Physics, Yale University, 217 Prospect Street, New Haven, CT 06520, USA

²² Space Telescope Science Institute, Baltimore, MD 21218, USA

²³ Department of Physics and Astronomy, Johns Hopkins University, Baltimore, MD 21218, USA

²⁴ University of Southern California, Los Angeles, CA 90089, USA

²⁵ Space Telescope Science Institute, 3700 San Martin Drive, Baltimore, MD 21218, USA

²⁶ Astronomy Program, Department of Physics and Astronomy, Seoul National University, 1 Gwanak-ro, Gwanak-gu, Seoul 08826, Republic of Korea

²⁷ SNU Astronomy Research Center, Seoul National University, 1 Gwanak-ro, Gwanak-gu, Seoul 08826, Republic of Korea

²⁸ Academia Sinica Institute of Astronomy and Astrophysics (ASIAA), No. 1, Section 4, Roosevelt Road, Taipei 10617, Taiwan

²⁹ Kavli Institute for Particle Astrophysics and Cosmology (KIPAC), SLAC National Accelerator Laboratory, Stanford University, 2575 Sand Hill Road, Menlo Park, CA 94025, USA

³⁰ Department of Physics, University of California Merced, 5200 Lake Road, Merced, CA 95343, USA

Received 2024 February 15; revised 2024 July 1; accepted 2024 July 21; published 2024 October 4

Abstract

The Local Volume Complete Cluster Survey is an ongoing program to observe nearly a hundred low-redshift X-ray-luminous galaxy clusters (redshifts $0.03 < z < 0.12$ and X-ray luminosities in the 0.1–2.4 keV band $L_{X500c} > 10^{44} \text{ erg s}^{-1}$) with the Dark Energy Camera, capturing data in the u , g , r , i , z bands with a 5σ point source depth of approximately 25th–26th AB magnitudes. Here, we map the aperture masses in 58 galaxy cluster fields using weak gravitational lensing. These clusters span a variety of dynamical states, from nearly relaxed to merging systems, and approximately half of them have not been subject to detailed weak lensing analysis before. In each cluster field, we analyze the alignment between the 2D mass distribution described by the aperture mass map, the 2D red-sequence (RS) galaxy distribution, and the brightest cluster galaxy (BCG). We find that the orientations of the BCG and the RS distribution are strongly aligned throughout the interiors of the clusters: the median misalignment angle is 19° within 2 Mpc. We also observe the alignment between the orientations of the RS distribution and the overall cluster mass distribution (by a median difference of 32° within 1 Mpc), although this is constrained by galaxy shape noise and the limitations of our cluster sample size. These types of alignment suggest long-term dynamical evolution within the clusters over cosmic timescales.



Original content from this work may be used under the terms of the [Creative Commons Attribution 4.0 licence](https://creativecommons.org/licenses/by/4.0/). Any further distribution of this work must maintain attribution to the author(s) and the title of the work, journal citation and DOI.

Unified Astronomy Thesaurus concepts: [Weak gravitational lensing \(1797\)](#); [Astronomy data analysis \(1858\)](#); [Surveys \(1671\)](#); [Galaxy clusters \(584\)](#); [Observational cosmology \(1146\)](#); [Dark matter \(353\)](#)

1. Introduction

While clusters of galaxies are the largest gravitationally bound structures in the Universe, connections and interactions still exist between close pairs of clusters, traced by intercluster filaments that connect them. Although the direct detection of filaments has been achieved in a small number of clusters (Dietrich et al. 2012b; Jauzac et al. 2012), it is generally difficult to detect them without stacking data (Zhang et al. 2013). Low-redshift massive clusters provide opportunities to inspect and study filaments individually in high resolution because of their proximity (Haines et al. 2018).

The different components of a cluster—the central galaxy (CG) or the brightest cluster galaxy (BCG), the member galaxy distribution, the gas, and the dark matter—may come to display similar orientations as the cluster evolves. Such alignment in low- and medium-mass clusters has been analyzed statistically to study cluster triaxiality (Shin et al. 2018). The alignment is stronger in massive clusters and has been detected in individual clusters at medium redshift ($0.1 < z < 0.9$) with ground-based telescopes (Oguri et al. 2010; Herbonnet et al. 2019) or space telescopes (Donahue et al. 2016; Umetsu et al. 2018), but in relatively small samples. In addition, cluster pairs may show alignment between their matter distributions due to the large-scale tidal field. Low-redshift ($z \lesssim 0.1$) massive clusters would reveal those intra- or intercluster features individually and in more detail, which can be observed by even ground-based telescopes. Low-redshift clusters allow one to resolve halo substructures and facilitate studies of, e.g., the correlation between cluster substructure and galaxy population/evolution (McClintock et al. 2015).

Nearby clusters are also useful for cosmological studies by providing a low-redshift anchor for the scaling relations between the cluster mass and the observables at the late Universe. The evolution of halo mass function is sensitive to the cosmological parameters Ω_m and σ_8 at the high-mass end, where galaxy clusters reside, and thus clusters provide a key probe of dark energy (Albrecht et al. 2006; Allen et al. 2011; The LSST Dark Energy Science Collaboration et al. 2018). Building mass functions requires accurate mass measurements of clusters with unbiased selection. Most clusters in the Universe are not massive enough to produce significant gravitational lensing signals that overcome measurement noise, and their individual masses are difficult to be directly measured. However, their masses can be statistically inferred from scaling relations between the mass and the observables, e.g., member galaxy richness and gas properties (X-ray emission or the Sunyaev–Zel’dovich (SZ) effect). Weak lensing (WL), on the other hand, yields unbiased mass estimates over a large ensemble of clusters and thus permits calibration of those scaling relations (McClintock et al. 2019; Miyatake et al. 2019; Umetsu 2020). To construct a scaling relation, the cluster sample needs to be complete and span a wide range of dynamical states to avoid biased cosmological inference (Kettula et al. 2015).

In the past, it was difficult to study clusters at very low redshift via WL, because those clusters require high-quality point-spread function (PSF) modeling over a large sky area and very deep observations to reduce shape noise as their lensing

signal ($\propto D_{ls}D_l$) is low compared to clusters at medium redshift. However, nowadays nearby clusters can be well captured by recently developed large aperture and large field-of-view (FoV) instruments, e.g., the Dark Energy Camera (DECam; FoV 2.2°) mounted on the 4 m Blanco Telescope at the Cerro Tololo Inter-American Observatory (CTIO), and the future LSST Camera (FoV 3.5°) mounted on the 8.4 m Simonyi Survey Telescope at the Rubin Observatory. The large aperture enables fast and deep observations of hundreds of thousands of galaxies at the same time. Meanwhile, recent tools strengthen the PSF modeling over a large FoV, which improves the shape measurements for lensing analysis (Bosch et al. 2018). As a result, accurate lensing measurements of nearby clusters have become easier to achieve than in earlier years. DECam has already proved its excellent performance in the recently completed Dark Energy Survey (DES; Dark Energy Survey Collaboration et al. 2016), and as a comparison, the 10 yr LSST (Ivezić et al. 2019) will be ~ 3 mag deeper over an approximately three times larger sky footprint. In addition to optical observations, X-ray observations (e.g., Chandra, XMM/Newton, eROSITA) and SZ observations (e.g., Planck) provide a vast amount of information about the hot gas in nearby clusters.

We proposed the Local Volume Complete Cluster Survey (LoVoCCS; Proposal ID: 2019A-0308; PI: Ian Dell’Antonio) to observe a volume-complete sample of 107 nearby X-ray luminous clusters ($0.03 < z < 0.12$; $[0.1–2.4 \text{ keV}] L_{X500c} > 10^{44} \text{ erg s}^{-1}$; $M_{500c} \gtrsim 2 \times 10^{14} M_\odot$, $M_{200c} \gtrsim 3 \times 10^{14} M_\odot$) in low Galactic extinction fields using the DECam u , g , r , i , z bands. Here, the subscript 500 c (200 c) means the mass within a radius where the average overdensity is 500 (200) times the critical density at that redshift; the mass M_{500c} is given by Piffaretti et al. (2011) and we convert it to M_{200c} using typical Navarro–Frenk–White (NFW) halos (Navarro et al. 1997; Child et al. 2018). The survey started in 2019 and is expected to conclude by 2024. The deep coadded images of each cluster field have reached LSST Years 1–2 depth (~ 1 mag deeper than DES; Appendix A) more than 2 yr prior to the LSST Y1 data release. Additionally, $\gtrsim 10$ northern LoVoCCS clusters will not be fully covered by LSST (especially the ones outside the North Ecliptic Spur and at high declination). These coadded images can also serve as a zeroth-year template for LSST transient studies.

We observed the cluster sample in uniform depth but prioritized clusters that have higher X-ray luminosities. Although delayed by the pandemic and inclement weather, we have finished the observation of 83 clusters (complete to the top 52 clusters in terms of X-ray luminosity) and obtained 87% of the survey data (including archival data), as of the submission of this paper (Figure 1). In addition, we have been awarded further DECam time to survey a sample of Planck SZ clusters near the LoVoCCS X-ray luminosity cut to increase the SZ completeness (Proposal ID: 2022A-658443; PI: Ian Dell’Antonio), and Hyper Suprime-Cam (HSC) time to observe northern clusters selected by the same criteria aiming to improve the all-sky completeness (Proposal ID: S20A-127, S23B-105, S24A-81; PI: Hironao Miyatake).

We presented the survey background, pipeline, and early science results in our first LoVoCCS paper (Fu et al. 2022, hereafter Paper I). In this second paper, we study a sample of

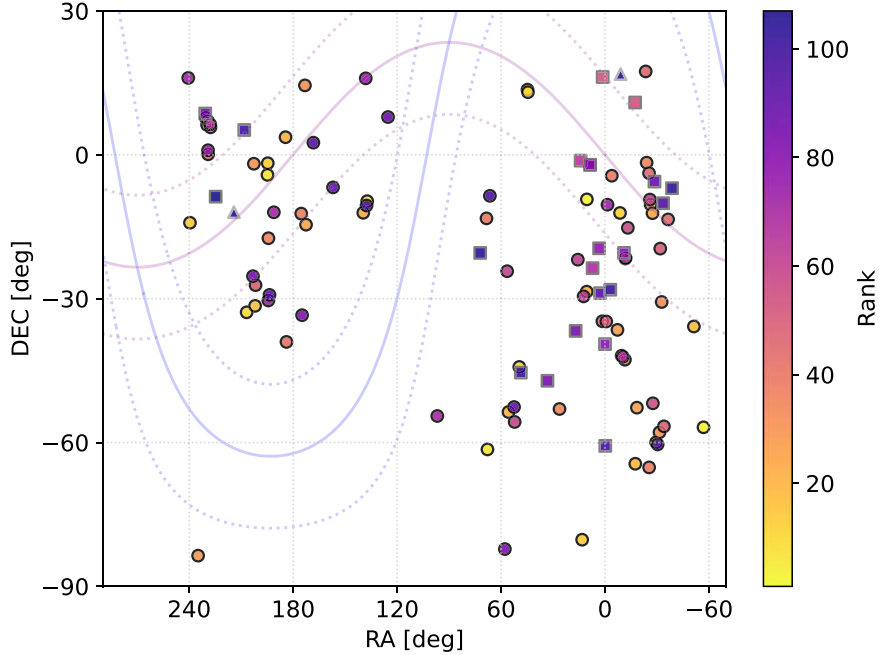


Figure 1. Celestial distribution of LoVoCCS clusters with their ranks and observation completeness (107 clusters in total). The black-edge circles denote clusters that have finished observation (83 clusters). The gray-edge squares denote clusters that were partially observed (22 clusters). The light-gray-edge triangles denote clusters that have not been observed (two clusters). The marker face color shows the cluster rank. A higher rank corresponds to a higher X-ray luminosity (a brighter color in the figure); high-rank clusters are generally more complete in observation. The purple and blue solid curves represent the ecliptic plane and the Milky Way galactic plane, respectively, and the dashed curves show $\pm 15^\circ$ from the planes.

58 clusters from LoVoCCS (Section 2), with a focus on the mass distributions and galaxy distributions in these clusters. About half of the cluster sample ($\gtrsim 24$ clusters) have not been studied in detail via WL previously, and the rest provide comparisons of our study with previously reported results. In this work, we analyze the performance of the photometric redshift measurement and improve the quality check procedure in our pipeline, and we extend the pipeline by adding steps to construct the distribution of red-sequence (RS) galaxies and to study cluster triaxiality by measuring the orientations and positions of the BCG, the RS galaxy distribution, and the lensing mass distribution on the plane of sky (Section 3). In Section 4, we present the optical image overlaid with the mass map and RS distribution contours of each cluster (or cluster pair/group), and we compare the orientations and locations of those cluster components (BCG, galaxy distribution, and mass distribution) in individual clusters as a function of cluster evolution stage. We then discuss our results in Section 5 and summarize the paper in Section 6.

Throughout this paper, we use the same cosmological parameters as Paper I: flat Λ CDM $H_0 = 71 \text{ km s}^{-1} \text{ Mpc}^{-1}$, $\Omega_m = 0.2648$; switching between commonly used values slightly changes the angular diameter distances and luminosity distances in this work (by $\lesssim 2\%$).

2. Data Set

Our sample of 58 clusters covers a large variety of X-ray luminosities (and therefore masses)³¹, redshifts

($0.04 < z < 0.12$), and dynamical states (perturbed or nearly relaxed). We rank all LoVoCCS clusters by X-ray luminosity (Piffaretti et al. 2011) from one to 107. The 13 highest-ranked LoVoCCS clusters are included in this work, and the lowest rank in the sample is 99 (A3825). These 58 clusters are exposure-time complete in LoVoCCS and have high-quality processing results. We give a list of public data sets used for coaddition in Appendix B. Each cluster is covered by $\gtrsim 100$ exposures. As mentioned earlier, we summarize the 5σ coadded depth of these cluster fields in Appendix A; the median depth values are 25–26th PSF magnitudes for point objects in the u, g, r, i, z bands, and the CModel magnitudes for extended objects are ~ 0.3 mag shallower. The point and extended objects are separated by the LSST Science Pipelines (LSP) parameter extendedness in the r band, which is the band for our shape measurements for lensing analysis (we require seeing $\lesssim 1''$), and we have used the LSP flags `base_PsfFlux_flag` and `modelfit_CModel_flag` to select objects that have high-quality photometric measurements. We include archival Y -band data in the processing for photometric redshift measurements.

3. Methods

The LoVoCCS pipeline has been presented in Paper I. Here we briefly summarize the pipeline (Section 3.1), and emphasize the steps that have been taken to improve it in the remainder of this section. We describe the performance of our photometric redshift measurements (Section 3.2) and mass map construction (Section 3.3); the new steps taken in performing the RS galaxy analysis (Section 3.4) and cluster triaxiality analysis (Section 3.5); and the improvements in our data quality checks (Section 3.6).

³¹ X-ray luminosity in the 0.1–2.4 keV band: $1.1 \times 10^{44} \text{ erg s}^{-1} < L_{X500c} < 8.7 \times 10^{44} \text{ erg s}^{-1}$; mass based on the X-ray emission: $2.0 \times 10^{14} M_\odot \lesssim M_{500c} \lesssim 7.3 \times 10^{14} M_\odot$ (Piffaretti et al. 2011). <https://heasarc.gsfc.nasa.gov/W3Browse/roseat/mcxc.html>.

3.1. Pipeline Steps

We require a framework that allows us to consistently analyze the full diversity of virialized and merging clusters in LoVoCCS. For this, we use the LSP software³² version 19.0.0 to first process the raw data and then use our own pipeline to analyze the LSP data products of each cluster uniformly. The LSP software enables us to use the latest algorithms designed for future LSST data. The output images and catalogs are therefore compatible with the LSST data products, which simplifies and enables future synergies. The LSP software has the ability to process the data from different instruments, including DECam, Subaru/HSC, and Canada-France-Hawaii Telescope/MegaCam, in a similar manner. The details of LSP have been described by Bosch et al. (2018).

In each cluster field, we first download the public DECam data from the NOIRLab Astro Data Archive.³³ We use the LSP to detrend the raw DECam exposures at individual CCDs. The astrometry and photometry of each CCD are calibrated against external stellar catalogs—Gaia (Gaia Collaboration et al. 2016, 2018; Gaia Collaboration 2018) for astrometric calibration, and Pan-STARRS1 (PS1; Chambers et al. 2016; STScI 2022), SkyMapper (Australian National University 2017; Wolf et al. 2018; Australian National University 2019; Onken et al. 2019), and Sloan Digital Sky Survey (SDSS; Alam et al. 2015) for photometric calibration. We then select high-quality CCD exposures by the seeing measured on the processed images: median ellipticity <0.13 , FWHM <1.16 in the r band (for lensing analysis), and ellipticity <0.33 , FWHM <1.74 in other bands. We improve the astrometry and photometry of those exposures by calibrating their catalogs jointly. Next, the exposures are mapped onto $4k \times 4k$ pixel patches ($0.3^\circ \times 0.3^\circ$, 0.263 pixel^{-1}), and adjacent patches have an additional 100 pixel overlap. The exposures are then stacked on each patch and in each band. After stacking, the LSP detects, deblends, measures objects on the coadded images, and performs forced photometry among different bands on each object. We use the shape information measured on the coadded r -band image for lensing analysis, and we use forced photometry to obtain the color information of each object.

After the LSP steps, we correct for the Galactic extinction using the dust reddening map (Schlegel et al. 1998; Schlafly & Finkbeiner 2011; IRSA 2022), and further calibrate the magnitude zero-points in the coadd catalog (measured from the coadded images) using the model color terms and the color–color stellar locus. We then measure photometric redshifts, build lensing mass maps and shear profiles, derive lensing masses, and check the data product quality. In this work, we also add steps to construct RS galaxy distributions and cluster triaxiality metrics.

We adjust the pipeline in some special cases. The default angular cut on the CCD selection is 1.5° toward the cluster center, which results in 12×12 patches generally. In the field of A401 and A3558, we use larger angular cuts (1.8° and 2° , respectively) to include the nearby clusters that they are interacting with. For the A401/A399 field in the northern sky, since there is no SDSS coverage for the u -band photometric calibration, we build a synthetic reference catalog for the LSP based on the empirical color transformations between PS1

(deep observations in g and r) and DECam (u) in other cluster fields, and we further calibrate the u -band photometry in the coadd catalog using the model stellar locus of $g - r$ versus $u - g$ after the extinction correction; we find that this approach produces reasonable photometric redshifts compared to the spectroscopic redshifts.

3.2. Photometric Redshifts

In this work, we continue using the Bayesian photometric redshift (BPZ; Benítez 2000; Coe et al. 2006) algorithm to estimate galaxy photometric redshifts (photo-zs), and we compare the results with archival public spectroscopic redshifts (spec-zs) obtained from NASA/IPAC Extragalactic Database (NED; Helou et al. 1991; NED 2019).

As mentioned in Paper I, the photo- z outliers at low (true) redshift are mainly caused by the lack of archival u -band data on the periphery of cluster fields, blended objects, or special galaxy types/colors. However, the insufficiency of u -band data is rarely the case in the cluster central areas we observe for lensing analysis. After visual inspection, we find that the galaxy type assigned by BPZ is generally correct (we use a two-step interpolation between consecutive templates), and we also find that the spirals in clusters are more likely to have photo- z ’s biased high because they are redder than field galaxies due to quenching. The outliers also include cluster dwarf galaxies, which are more common in galaxies with blue BPZ galaxy types. Figure 2 shows an example of our photo- z quality: a comparison between the spec-zs and photo-zs of a clean sample of galaxies selected by $z_s < 1.5$, $\text{odds} > 0.95$, $\chi^2_{\text{mod}} < 1$, and covered by the u band; the photo- z uncertainty and the outlier rate are both at a few percent. Here, odds and χ^2_{mod} give the BPZ probability concentration and closeness of fit, respectively. Note the archival spec- z data sets mostly focus on cluster member galaxies for dynamical analysis.

In this work, we use a photo- z cut at the cluster redshift plus 0.1 to remove foreground galaxies, instead of a fixed cut at 0.15 used in Paper I. Therefore, the photo- z cut is different in different cluster fields. This change improves the lensing map signal-to-noise ratio (S/N) of our higher-redshift clusters by $\lesssim 10\%$. This change in mass map could be caused not only by the reduction of foreground galaxy contamination, but also by the high sensitivity to lensing signal of background galaxies at low redshift. Adding higher photo- z cuts can remove both foreground and background galaxies because of the photo- z noise—we seek to find a *balance* between the lensing signal and shape noise. In Paper I, under the original photo- z cut, we estimated that photo- z outliers could dilute the lensing signal by a few percent. As more foreground galaxies are removed under the new photo- z cut, we estimate the bias of mass maps in this work introduced by photo- z errors is even smaller (approximately percent level). We note that in Figure 2 there is a cloud of galaxies at $z_s \sim 0.2$ with $z_p \sim 0.25$ (these are likely dusty/quenched), however these galaxies are mainly behind our cluster sample ($z \lesssim 0.1$), and thus we do not expect their presence to affect our mass maps significantly. As in Paper I, we also remove sources at photo- z higher than 1.4 because their shape measurements can be noisier.

In Figure 2, the galaxies have magnitudes $i \lesssim 24$, which is generally brighter compared to the whole sample for lensing analysis. For the fainter lensing sources, their photo- z errors could be larger than the galaxies we use for the spec- z versus photo- z comparison. However, the photo- z bias does not occur

³² <https://pipelines.lsst.io>

³³ <https://astroarchive.noirlab.edu>

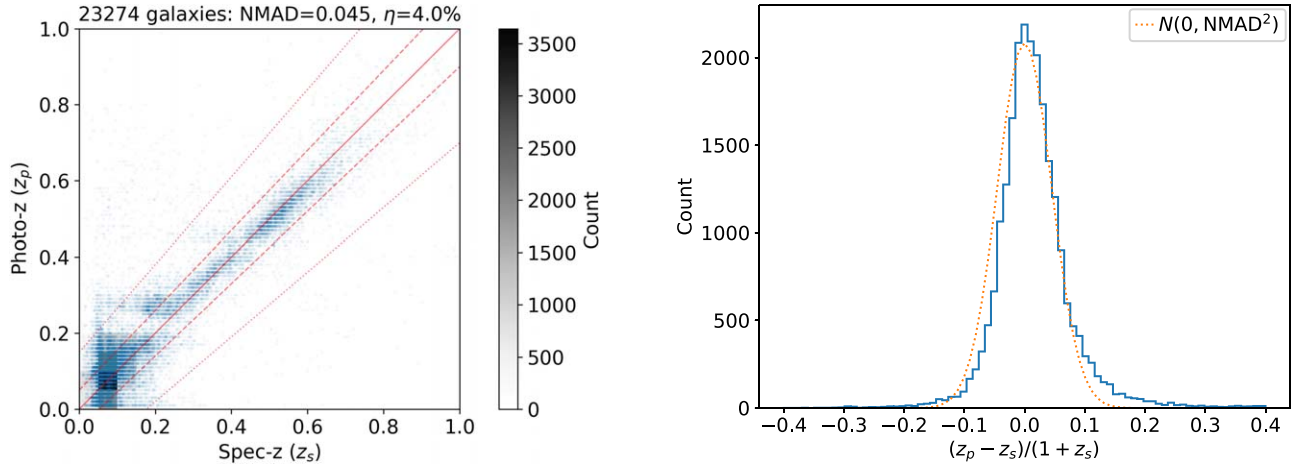


Figure 2. Comparison between the photo-zs (z_p) and spec-zs (z_s) in all cluster fields studied in this paper with metrics of the photo-z error $\Delta z = (z_p - z_s)/(1 + z_s)$. Left: the dotted, dashed, and solid lines represent biases of $|\Delta z| = 0.15, 0.05$, and 0, respectively. We use a step of 0.01 in BPZ. The normalized-median absolute deviation ($1.48 \times \text{median}\{|\Delta z|\}$; NMAD) shows an estimation of the photo-z uncertainty, and the percentage of galaxies that have $|\Delta z| > 0.15$ gives the outlier rate η . Right: the blue solid curve shows the distribution of Δz , which is nearly a Gaussian $N(0, \text{NMAD}^2)$, the orange dotted curve; the small bias is mainly caused by the low-z galaxies (mostly cluster members) at $z_s \lesssim 0.2$.

in a specific sky area but occurs everywhere. Thus, we expect that the photo-z bias of faint objects will not materially affect the 2D structure reconstruction. Also, the clusters studied in this work are at low redshift, and most background sources are at high redshift. For low-z clusters, the lensing signal is not sensitive to the exact redshift of the high-z sources—the reduced shear (more specifically, the lensing distance ratio D_{LS}/D_S) changes slowly with the (true) redshift (e.g., Applegate et al. 2014). In addition, faint objects are unlikely to be foreground galaxies of these low-z clusters, which means the foreground contamination caused by faint objects is small.

To further filter out foreground galaxies, we examined the inclusion of archival photometry in other wavelength bands. Given the depth, footprint, and seeing of archival data, we consider adding external near-infrared (NIR) photometry to remove the member/low-z galaxies (instead of increasing the wavelength coverage of background sources). Those foreground galaxies are relatively larger and brighter than the background sources, and thus, they are unlikely to be affected by the seeing and depth of those external catalogs. We match the Legacy Surveys + Wide-field Infrared Survey Explorer (LS + WISE) forced photometry catalog from the DESI Legacy Imaging Surveys (Dey et al. 2019) and the VISTA Hemisphere Survey (VHS) catalog (McMahon 2011; McMahon et al. 2013)³⁴ with the LoVoCCS catalog and the NED spec-z catalog. We find that in the color–color space of, e.g., $z - w_1$ versus $w_1 - w_2$, $Y - J$ versus $J - K_s$, no simple cut can fully separate those foreground galaxies ($z_s \lesssim 0.1$) from the others. Also, when comparing the mass maps with and without cuts on NIR colors, we find no significant difference. Therefore, in the following analysis we only use the photometry from LoVoCCS. Another approach to the removal of foreground galaxies is to use a machine learning photo-z algorithm, which takes the *morphology* and *special colors* of cluster members into account—we will explore this in the future.

In fact, as it turns out, the mass map morphology is not very sensitive to the photo-z selection as member galaxy shapes are randomly distributed in general; they do exhibit intrinsic

alignment (IA) caused by tidal fields, but we expect this to be a secondary effect compared to the cluster lensing signal. Similarly, we assume that the IA between background sources is a secondary effect as well and thus do not consider it when constructing mass maps. Additionally, we make cuts on the photo-z quality metrics ($\text{odds} > 0.95$ and $\chi^2_{\text{mod}} < 4$) before making mass maps to ensure the photo-z quality and to be consistent with the mass fitting step. The photo-z quality cuts reduce the median galaxy number density from $\sim 22 \text{ arcmin}^{-2}$ (shape and photometry cuts have been applied) to $\sim 8 \text{ arcmin}^{-2}$, and the photo-z value cut further reduces the source density to $\sim 7 \text{ arcmin}^{-2}$. Our test shows that including more sources using wider photo-z quality cuts does not significantly improve the S/N of mass maps, and the reason could be that the sources outside our quality cuts have noisier shape measurements.

3.3. Aperture Mass S/N Map

As in Paper I, we make quality cuts and conduct shear calibration on the HSM shapes (Hirata & Seljak 2003; Mandelbaum et al. 2005, 2018a) on the coadded catalog before analyzing the lensing signal. We then use the aperture mass statistics (Schneider 1996) to build lensing mass S/N maps via the Schirmer filter (Schirmer et al. 2004; Hatterscheidt et al. 2005; von der Linden et al. 2014). The aperture mass signal is a convolution between the convergence map (normalized surface mass density) and a circular (radially symmetric) weight function, and it is equivalent to a convolution between the tangential shear and a circular filter function (the Schirmer filter in this case). We approximate the tangential shear by the mean of per-galaxy reduced shear estimates derived from galaxy shapes, and we compute the mean within 100×100 pixel bins to reduce shape noise. The noise in the aperture mass mainly comes from the shape dispersion of source galaxies. Therefore, both the signal and noise parts of the mass S/N map scale with the source galaxy shapes. The possible remaining biases (usually multiplicative) in the galaxy shapes caused by, e.g., blending, photo-z bias, shape measurement, can be mostly factored out in the S/N, and we thus consider them as secondary effects.

³⁴ We obtained the LS+WISE and VHS catalogs from the NOIRLab Astro Data Lab. <https://datalab.noirlab.edu/index.php>.

The S/N mass map shows how the underlying mass is concentrated. The Schirmer filter produces the highest S/N at an aperture center when the characteristic scale of the halo structure around that center is approximately one-tenth of the aperture radius. Thus, we vary the aperture radius starting from 3k pixels with steps of 1k pixels to determine the mass map that best captures the cluster-scale structure. In general, we choose the aperture that maximizes the peak S/N in the mass map; if the corresponding scale size is too small or large, we consider a local maximum where the aperture corresponds to the size of a normal cluster. Also, the morphology, in particular, the orientation of the projected halo should not be strongly affected by the convolution during the mass map construction, given the symmetry of the weight function. Using mock lensing catalogs, we verified that the mass map algorithm recovered elliptical halo orientations (Appendix C).

Most of our mass maps are built based on the catalogs of central 6×6 patches ($24k \times 24k$ pixels; $1.8^\circ \times 1.8^\circ$) divided by the LSP. For the cluster A3558, we consider the catalog of the full 15×15 patches to study the nearby structure in the Shapley supercluster, but we only present the central mass map to ensure the quality. The flat sky approximation is still valid in these sky regions. In Section 4.1, we present only the (curl-free) E-mode maps derived from the tangential shear toward aperture centers. We find that reassuringly, the corresponding B-mode maps derived from the cross component show no clear patterns, especially near the cluster centers.

The large angular sizes of the low-z clusters in LoVoCCS occasionally encompass background clusters in the field, which may contaminate the lensing signal of the cluster of interest. If we select only the source galaxies that lie in between the foreground cluster and the background cluster, it would severely penalize the S/N. Hence, we retain background clusters when constructing the mass maps, rather than using cuts on source galaxy redshifts, to obtain sufficient S/N. Moreover, these background clusters usually span an angular region much smaller than the foreground one, and thus, we expect that they only affect cluster substructure detection in general. However, if the background cluster is very close to the foreground cluster center, we remove the background source galaxies closer to the background cluster (e.g., in A3128) because the background cluster may strongly affect the mass peak position and S/N of the cluster of interest. In the future, we plan to use external cluster catalogs or run cluster finders (based on optical concentration, RS, or X-ray/SZ) to locate background clusters, which is important for accurately determining the foreground cluster mass.

As mentioned earlier, we use LSP flags to select high-quality objects for analysis. We find that those flags generally remove objects affected by saturated stars and satellite trails, and the cluster central morphology does not change greatly after new masks are added around bright stars; we give more examples in Section 4.1 when we study individual clusters.

3.4. RS Galaxy Distribution

Galaxy clusters contain a large population of red elliptical/early-type galaxies formed by galaxy merging and quenching. In the color-magnitude diagram (CMD), they exhibit a characteristic RS, which results from the unique features in their spectral energy distributions (SED), especially the 4000\AA break caused by old stars and metal absorption lines. The RS galaxies tend to be redder and brighter near the cluster

center because of their dynamical (infalling/merging) processes and quenching history. These RS galaxies trace the overall matter distributions in clusters, and they are closely related to luminous red galaxies (LRGs). LRGs are common tracers of the large-scale structure (LSS) and delineate the connections between clusters.

In this work, we include a new pipeline step that builds an RS galaxy distribution in each cluster field based on its CMD. To best locate the RS in CMD, one can use the colors of spectroscopically confirmed cluster member galaxies. This method works well in those LoVoCCS clusters with adequate spec-z data; though the archival spec-zs in the LoVoCCS cluster fields are limited, most of them are member galaxy spec-zs. However, those spec-zs are mainly from bright galaxies, and in some clusters, the number of member spec-zs is not sufficient ($\lesssim 200$) to allow reliable data fitting in the CMD. In addition, photo-z does not work very well at low redshift and is not so useful for picking out cluster galaxies. Therefore, we also use all galaxies with valid photometry to locate the RS in the CMD. We provide more details of our algorithms below, and we use the CModel magnitudes for galaxies. In Appendix D, we show examples of RS detection and selection.

First, the archival spec-zs are accessed from NED (Section 3.2 and Paper I) and matched with the LoVoCCS galaxy photometric catalog. The cluster member galaxies are selected by $|z_s - z_{cl}| < 0.01$, where z_{cl} is the cluster redshift. Then, we consider both colors $g - r$ and $r - i$ because of their wavelength coverage and depth, and we find that making cuts on two colors instead of one color gives a better selection of RS galaxies. We use the i -band magnitude as a luminosity proxy because of its depth and small K-correction ($\lesssim 0.05$ mag based on model SEDs used in BPZ), which simplifies the comparison between LoVoCCS clusters, and we thus skip the K-correction in the following analysis.

Next, we detect the RS in the CMD of spectroscopically selected cluster members and fit the data. We divide the i -band magnitude from 13.5 to 19.5 with a step of 0.3 mag, the $g - r$ color from 0.65 to 1.0 mag with a step of 0.06 mag, and the $r - i$ color from 0.25 to 0.45 with a step of 0.04 mag; each color step approximates to the corresponding RS scatter. We then go through the i -band magnitude bins, and for each magnitude bin, we generate a histogram of the $g - r$ color and find the peak among the color bins; we skip the magnitude bin if the number of galaxies inside is below 10. Then, the i -band magnitude bins and their corresponding $g - r$ color peaks are fitted by a straight line via `scipy.optimize.least_squares`, and we use a loss function `soft_l1` to reduce outliers. After fitting, we select galaxies that are 0.09 mag around the fitted $g - r$ color of their i -band magnitudes, and within those selected galaxies, we repeat the above steps but on the $r - i$ color to make another fit. We found that fitting the selected galaxies rather than all galaxies resulted in better RS detection.

We repeat the same procedure on the whole galaxy photometric catalog and increase the number limit of galaxies per magnitude bin to 15. Then, the higher quality of the spectroscopic and photometric fits is selected through visualization and comparison; the former usually gives a better result when the spec-z data is sufficient. However, only approximately one-quarter of the cluster sample has enough spec-zs. On the other hand, those clusters provide validation for the

performance of the photometric fit—the completeness/purity between the RS selections (see the magnitude and color cuts below) based on the spectroscopic fit and the photometric fit is $\gtrsim 90\%$. In some special cases, we also adjust parameters, e.g., the step, the number limit per bin, or the bright end of the i magnitude, to improve the fit. The result shows that in our cluster sample, the typical RS fit slopes are ~ -0.04 and ~ -0.02 in $g - r$ and $r - i$ versus i , respectively, with no obvious dependence on redshift. Additionally, the RS seems to be more clear and concentrated (and thus easier to locate and fit) in the CMD of more relaxed clusters, possibly resulting from the cluster evolution.

After we obtain the best RS fit, we make color and magnitude cuts on the whole galaxy photometric catalog. We select galaxies that are < 0.09 mag and < 0.06 mag around the fitted $g - r$ and $r - i$ colors, respectively; we use those scatter cuts to deal with the RS noise. We also make an i -magnitude cut changing with the cluster redshift, which leads to a fixed luminosity limit and simplifies direct comparison among clusters. The fiducial cutoff is $i = 20$ for a cluster at redshift $z = 0.08$ (approximately the median of our cluster sample and LoVoCCS), and we vary the i -band cut based on the cluster luminosity distance (the difference among clusters is $\lesssim 2.5$ mag, much larger than the K-correction). This i -band limit corresponds to an absolute magnitude limit at $M_i \sim -17.8$. We set this limit based on the spec-z data depth for the RS fit, and also to remove faint background objects since our clusters are at low redshift. We expect that the RS contamination from background clusters is low, given the color and magnitude cuts. In addition, our method directly detects the RS in the CMD without any training sets.

We make a further cut on the galaxy sample (after the color and magnitude cuts above) before building the RS density map: we use BPZ galaxy type $t_b==1$ to select a sample of elliptical galaxies. After checking spec-zs and optical images, we find that this cut removes foreground/background galaxies within the color ranges and gives a clean sample of bright cluster member galaxies. We note that varying the t_b cut from 1 (elliptical) to 2 (spiral Sbc) does not strongly affect the RS galaxy distribution morphology, especially near the cluster center. After the selection, the RS magnitude distribution is close to a Gaussian, and the (apparent) magnitude histogram peak (about 3 mag from the magnitude cut; $M_i \sim -21$) changes with the cluster redshift.

Once we have a clean sample of RS galaxies, we compute their 2D distribution by kernel density estimation (KDE) to get the RS density map. Similar to the construction of mass maps, we generally consider the field of central 6×6 patches ($24k \times 24k$ pixels), and count the galaxy number in 100×100 pixel bins to reduce noise. We also remove a foreground/background galaxy number density estimated by the density within $2k$ pixels from the field edge (half of a patch); this density is not high because of the previous selections on the galaxy color and type.

To make the final RS galaxy distribution, the galaxy count grid is then convolved with a 2D Gaussian with a standard deviation σ of 200 kpc (KDE). This smoothing length is chosen to estimate the RS distribution in the cluster and is fixed so that the RS maps of clusters at different redshifts are comparable. Note that our RS maps are derived from only the number density and are not magnitude nor flux weighted. The resulting RS map for each cluster is presented in Section 4.1.

3.5. Triaxiality: Orientation and Centering Analysis

We study cluster triaxiality by analyzing the orientations and positions of the 2D mass distribution, RS galaxy distribution, and BCG. The BCG and cluster member galaxy distribution can trace the (nonspherical) dark matter distribution and the total mass distribution—they tend to have similar orientations (e.g., Herbonnet et al. 2019). For low and medium-mass clusters, stacking cluster profiles aligned with the BCG or member galaxy distribution can reveal the cluster triaxiality (e.g., Shin et al. 2018; Fu et al. 2024). For high-mass clusters (like the LoVoCCS sample studied in this work), those types of orientation alignment are less noisier in observations and may be visible in individual cluster fields.

Measuring the cluster ellipticity is more difficult than measuring the orientation angle on the plane of sky. For example, measuring the ellipticity of the mass distribution can be affected by the shear bias or the convolution in the mass map construction; the same measurement on the galaxy distribution can be affected by the galaxy population; the measurement on the BCG can be affected by the intracluster light (ICL). In addition, the ellipticity measurement may also vary with the cluster radius. However, measuring their orientations is less sensitive to these factors noted above. Therefore, in this work, we only measure the orientation angles.

We also compare the BCG centroid and the map peaks. In relaxed clusters, it has been claimed that the offset between the BCG and the mass center can provide constraints on self-interacting dark matter (SIDM; Kim et al. 2017; Harvey et al. 2019), while in perturbed clusters, the offset may result naturally from merging process or projection effects. The mass center can be traced by, e.g., the X-ray emission or statistically the lensing mass map.

We summarize our measured angles and centers of the 2D distributions and the BCG of each cluster in Tables 4 and 5 (Appendix E), and we give details of our measurement method below.

BCG. To carry out a more flexible measurement than the LSP, we first crop a $\sim 0.4 \times 0.4$ Mpc region around the BCG on the optical r -band coadded image to reduce neighboring structures, e.g., bright stars/galaxies or ICL. Then we use Source Extractor (SExtractor; Bertin & Arnouts 1996) with the detection threshold from 6σ to 35σ and a step of 2σ to detect and measure objects. We then pick the object with the largest area (as the BCG) under each threshold and take its median values of the coordinates (X_IMAGE and Y_IMAGE) and the angles ($THETA_IMAGE$). As those galaxies have angular sizes much larger than the PSF, we expect that the systematics caused by PSF are minimal. After visual inspections, we find that this process further reduces the effect of ICL and noise from blended objects but still gives the BCG orientation near the galaxy's outer envelope. Note if a cluster has multiple bright central galaxies, we pick the brightest one with the largest area.

Mass Map. In Section 4.1, we present the best mass S/N map of each cluster, which is under the aperture that maximizes the S/N of the cluster-scale structure. Starting from that mass map, we first locate the mass map peak within 0.2° of the BCG mentioned above. Then, we consider radial distance cuts of 0.5, 1.0, and 2.0 Mpc from that peak on the mass map; they give the properties near the cluster center, within the cluster edge, and within the nearby LSS, respectively. We skip the region further out because the signal is low and the contamination of

(projected) neighboring structure is strong there, and it is close to the observation field edge of clusters at very low redshift. Also, in some cluster fields, the map could be “rounder” at larger radii, which makes the angle measurement difficult. At each radial cut, we make small perturbations on the cut from -10% to 10% with a step of 2% , measure an angle in individual cropped mass maps, and take their median to reduce noise. The angle is computed by the second moments (similar to the SExtractor algorithm³⁵)—in Equations (1), (2), and (3), i is the pixel index, m_i is the mass map pixel value.

$$M_\alpha = \sum_i m_i \alpha_i / \sum_i m_i; \alpha = x \text{ or } y \quad (1)$$

$$M_{\alpha\beta} = \sum_i m_i \alpha_i \beta_i / \sum_i m_i - M_\alpha M_\beta; \alpha, \beta = x \text{ or } y \quad (2)$$

$$\theta = \frac{1}{2} \arctan \left(\frac{2M_{xy}}{M_{xx} - M_{yy}} \right). \quad (3)$$

RS Galaxy Map. The method for measuring the orientation angle and peak of the RS distribution is similar to that used for the mass map above—we replace the mass map with the RS galaxy map.

In Sections 4.2 and 4.3, we compare the orientations and centers, respectively, of the BCG, mass, and RS distributions of each cluster in our sample and study their statistics.

3.6. Data Product Quality Check

We use a “quality check” step in the pipeline to examine the quality of our data products by analyzing the statistics of representative quantities. The major improvement in our quality check step is evaluating the star-galaxy shape correlation as a function of distance. In Paper I, we use shape correlations between the stars used for the PSF modeling and the galaxies used for the lensing analysis to estimate the PSF modeling error. In this work, we improve the calculation of shape correlations by using TreeCorr³⁶ (Jarvis et al. 2004). TreeCorr is implemented in C++ and uses a tree structure to divide the catalog into small cells. It takes the mean values in the cells that are greatly separated to compute the correlation for that distance bin, instead of using individual pairs of objects in that bin. It thus saves the computing resources. Therefore, we can reach deeper magnitudes for galaxies ($r < 26$), and we find that the star-galaxy shape correlation is $\lesssim 10^{-4}$, i.e., the PSF modeling error is $\lesssim 10\%$ of the reduced shear. We present more details of assessing the performance of PSF modeling and shape measurement using shape correlations in the Discussion (Section 5.1).

4. Results

4.1. Maps

We present an r -band coadded image with the aperture mass S/N map and RS galaxy distribution overlaid in each diagram, in Figures 3, 4, 5, 6, and 7—in total 54 diagrams for 58 clusters sorted by X-ray luminosity; among them four diagrams include multiple LoVoCCS clusters (A2029/A2033, A401/A399, A3827/A3825, and A2556/A2554). If two LoVoCCS clusters are shown in one diagram, we label it with the one that has the higher X-ray luminosity. Each diagram shows the central 4×4 patches ($16\text{k} \times 16\text{k}$ pixels; $1.2^\circ \times 1.2^\circ$) around the cluster

except the cluster pairs above and A3558 (the Shapley supercluster) to show the nearby structure. We use an arcsinh scaling to display both faint and bright features on the coadded image, and the local sky oversubtraction effect near bright and large objects is thus visible. Since the oversubtraction mainly affects the neighboring large-area and low-surface-brightness objects, we do not expect it to strongly bias the analysis of the WL signal and the detection of RS galaxies—the lensing sources have small sizes and the selected RS galaxies are bright.

In the following text, each paragraph is labeled by the LoVoCCS cluster(s) in the corresponding diagram, although other nearby/projected clusters could be included in the field as well. In each field, we compare the optical image with the 2D mass and galaxy distributions to study the origin of clumps in those distributions. The term “aperture size” refers to the Schirmer filter radius. Note that the maximal S/N mentioned in the following text is for the mass map peak within an aperture, and therefore, it is *lower* than the detection S/N of the whole cluster. Instead, the detection S/N can be estimated by the error bar of the shear profile or the lensing mass of the cluster (e.g., the S/N of lensing masses presented in Paper I). Also, we note that a few clusters have previous lensing mass measurements but no reported lensing mass maps. If a cluster has reported lensing mass measurement but no mass map in the literature, we do not count our map as a “first” lensing mass map in the following paragraphs because we do not know whether previous researchers have built a mass map for that cluster or not. But this indicates that the true number of first mass maps presented in this paper can be larger than what we report. Compared to these previous studies, our data set has larger wavelength coverage for better determination of galaxy types and redshifts, along with deeper observation and larger FoV for lensing analysis.

A2029/A2033. A2029 ($z = 0.077$) and A2033 ($z = 0.082$) have been widely studied using spectroscopic and lensing measurements in optical windows (e.g., Sohn et al. 2019; McCleary et al. 2020). Compared to the previous study of McCleary et al. (2020), this work includes more exposures to improve the depth (by ~ 1 mag for shape measurements) and uses a different pipeline for image processing and lensing analysis; our results are similar. The lensing effect comes from both A2029 and neighboring structures. Here, we use a large aperture (15k pixels in radius) where the S/N of the central peak is maximized (7.6σ) in the mass map, but the signal of the Southern Infalling Group (SIG) is smoothed out. The lensing signal of SIG reaches a maximum of 1.8σ at a small aperture (5k pixels), and the RS density clearly shows a concentration of galaxies at SIG. The RS map shows a density peak SE of A2033, which is also shown in the member distribution described by Sohn et al. (2019). We note that A2033 produces a stronger lensing effect than SIG, but has lower galaxy density than SIG, which is consistent with Sohn et al. (2019) as well. We show the central 6×6 patches ($24\text{k} \times 24\text{k}$ pixels; $1.8^\circ \times 1.8^\circ$) to include both clusters and nearby structures.

A401/A399. Previous studies using X-ray and SZ observations show that A401 ($z = 0.074$) and A399 ($z = 0.072$) form a premerging pair with a gas filament connecting the two (e.g., Akamatsu et al. 2017; Bonjean et al. 2018; Hincks et al. 2022). Because their redshift difference is small, it is difficult to separate the RS of individual clusters, and thus, we study their RS galaxy distributions together. We find a clear bridge of RS

³⁵ <https://astromatic.github.io/sextorator/Position.html>

³⁶ <https://github.com/rmjarvis/TreeCorr>

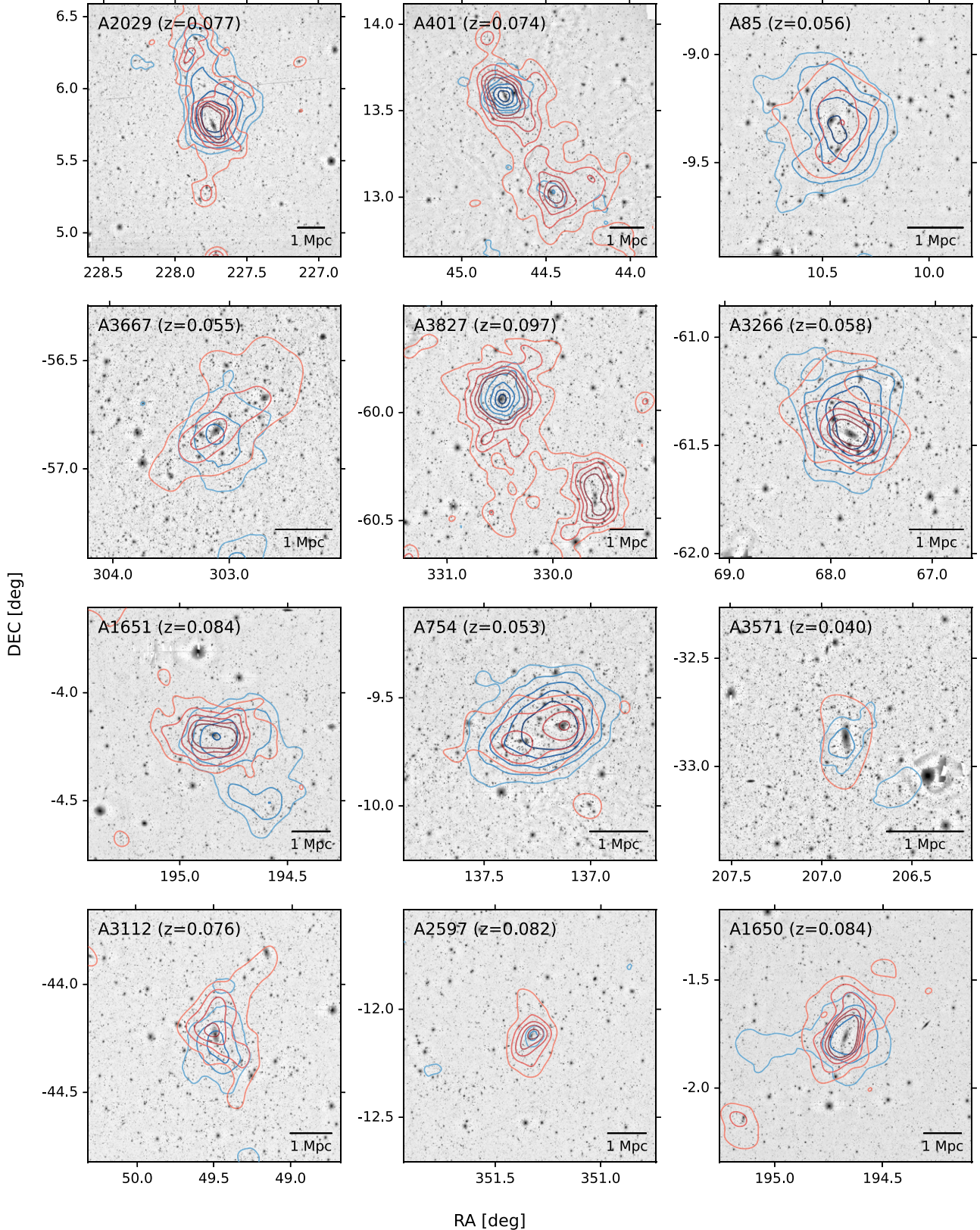


Figure 3. Grid of maps (Part I). In each diagram, the background is the inverted r -band coadded image; the blue contours stand for the aperture mass S/N, while the red contours represent the RS galaxy distribution. The mass S/N contours extend from 2σ to 6σ with a step of 1σ , and we choose an aperture that maximizes the S/N of the cluster-scale structure. The galaxy density contours extend from 0.024 to 0.12 per 100×100 pixels ($26.^{\prime\prime}3 \times 26.^{\prime\prime}3$) with a step of 0.024, and we use a smoothing length of 200 kpc (σ of a 2D Gaussian) in the KDE. The redshift is from SIMBAD (Wenger et al. 2000). The color schemes in all diagrams are the same; a darker color means a higher value.

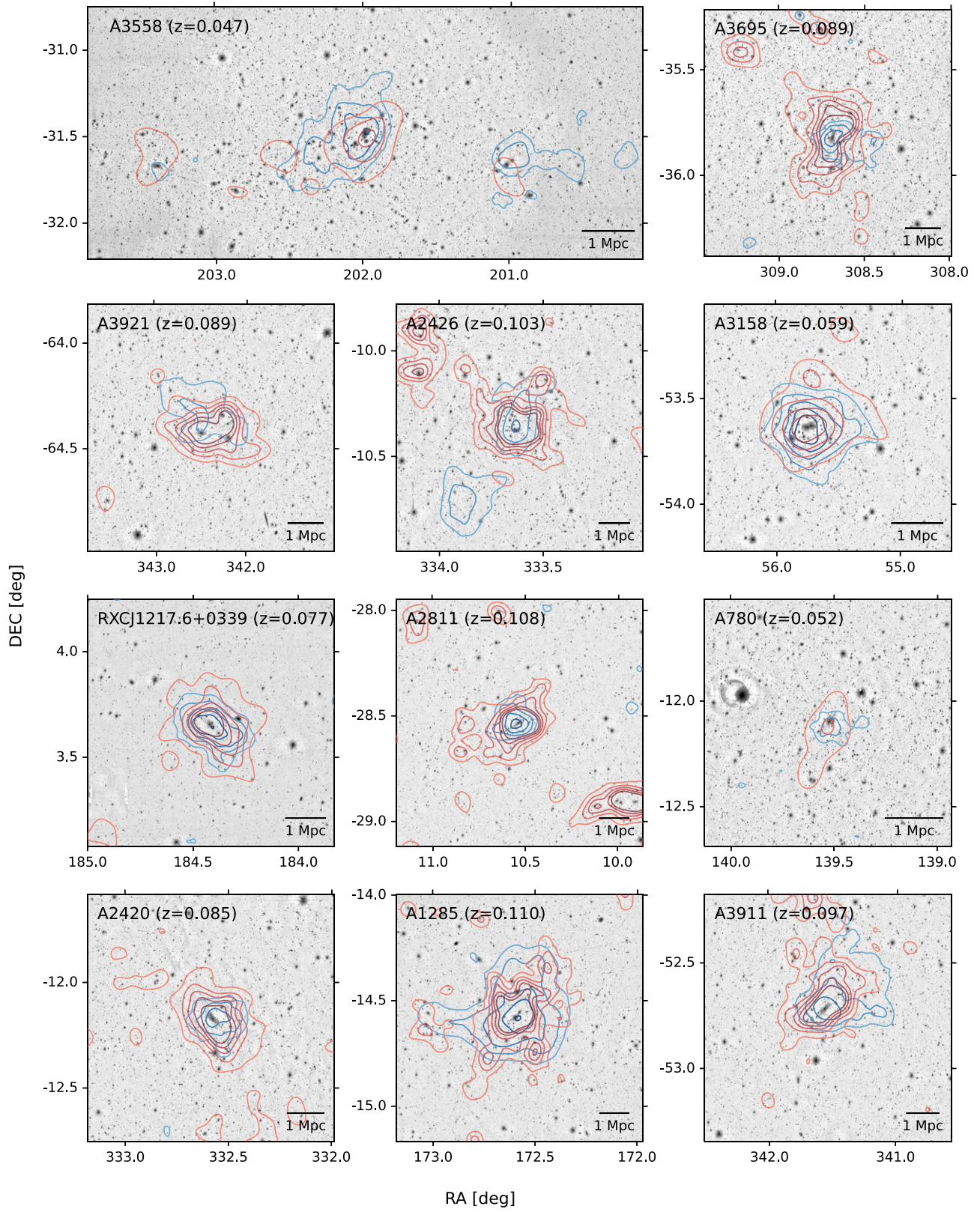


Figure 4. Grid of maps (Part II).

galaxies connecting the two clusters, which is consistent with the gas and previous galaxy analysis (Bonjean et al. 2018). Also, we present the first high-resolution lensing mass map of this cluster pair. We find that A401 has both a stronger lensing signal and higher RS galaxy density than A399, which is

similar to the gas distribution. Although we see no clear lensing signal from the filament, the mass contours of A399 (and the central galaxies of both clusters) roughly align with the direction connecting the two clusters. We use an aperture of 7k pixels in radius that maximizes the S/N peak of A401 (6.7σ) in

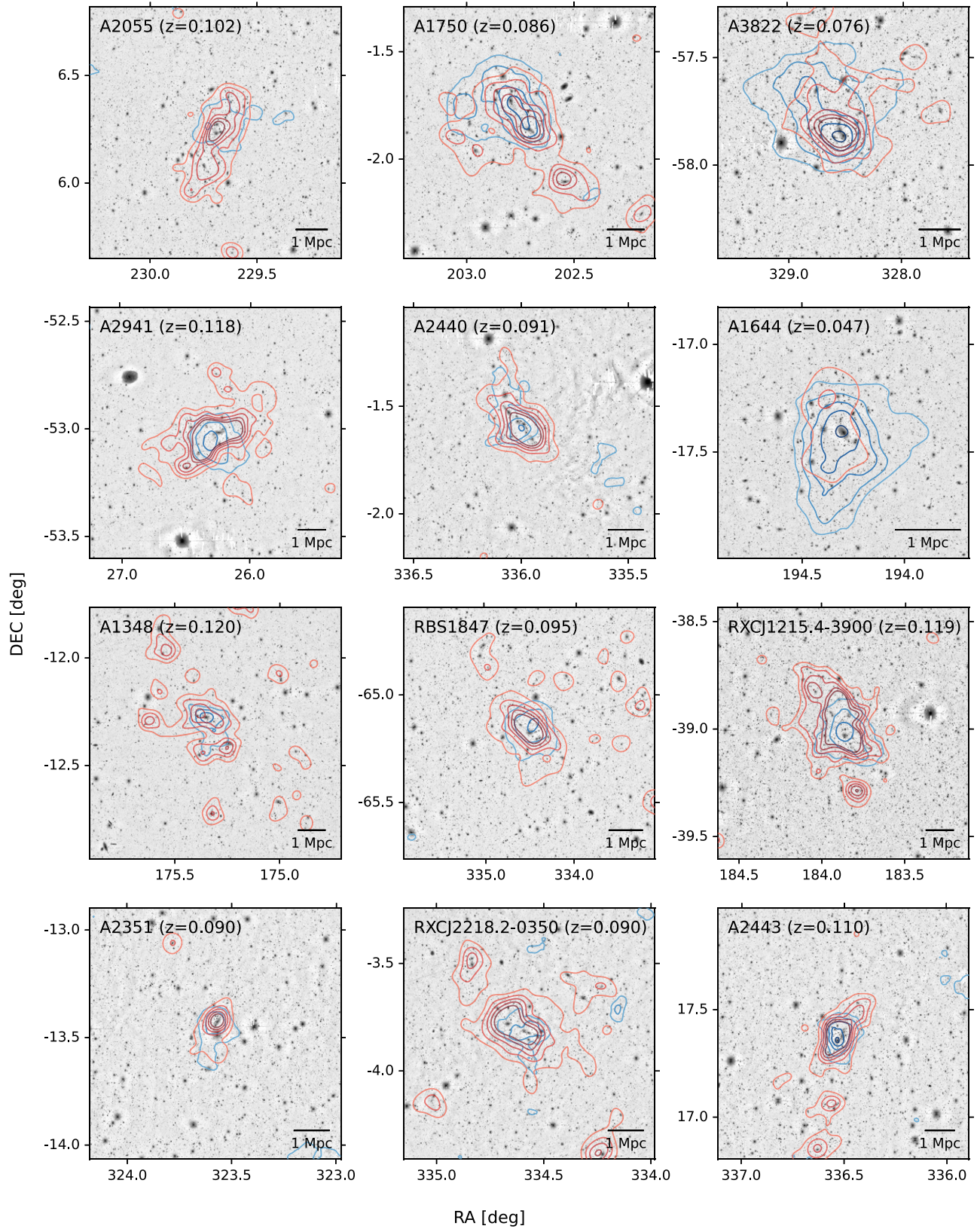


Figure 5. Grid of maps (Part III).

the mass map, while the S/N peak of A399 reaches the maximum at 3k pixels (3.4σ)—both lensing peaks are well detected despite cirrus and relatively high extinction (~ 0.3 mag in the r band) in this field. We present the central 5×5 patches ($20k \times 20k$ pixels; $1.5^\circ \times 1.5^\circ$) to show both clusters.

A85. A85 is a merging cluster and has been studied via WL by McCleary et al. (2020) and in Paper I. Here, we reanalyze it using the updated pipeline, and we also present its RS galaxy distribution (same for A3921 and A3911 below). The new mass map is consistent with the previous results, and our

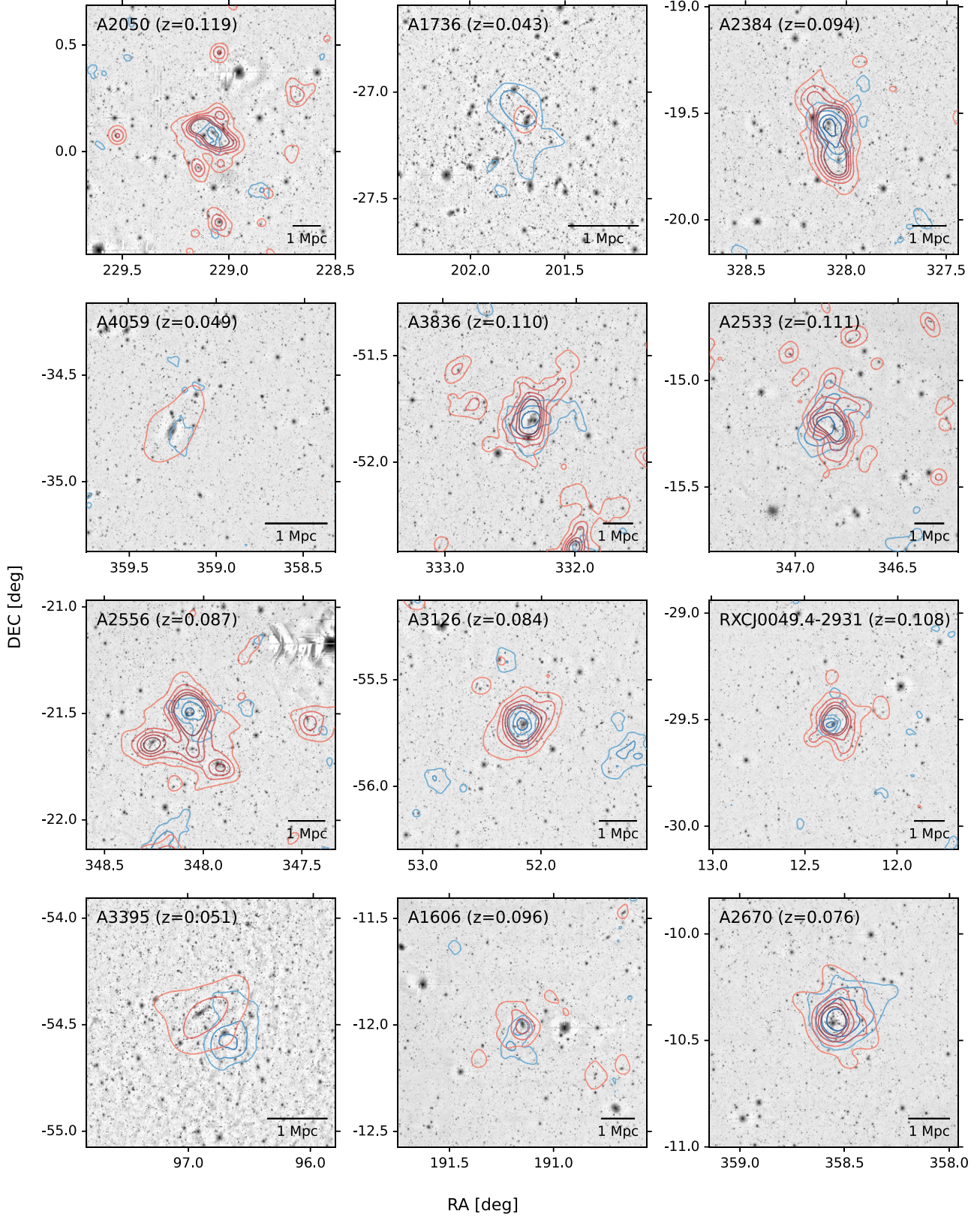


Figure 6. Grid of maps (Part IV).

catalog is ~ 1 mag deeper than the analysis of McCleary et al. (2020). We note that A85 has two central BCGs (northeast (NE) and southwest (SW)), and that the mass map S/N keeps increasing as the aperture grows because of the substructures

(two central clumps around respective BCGs). The SW peak has a slightly larger S/N than the NE one under small apertures (< 8 k pixels), indicating that it has a smaller physical size than the other, which also corresponds to a smaller BCG. We use an

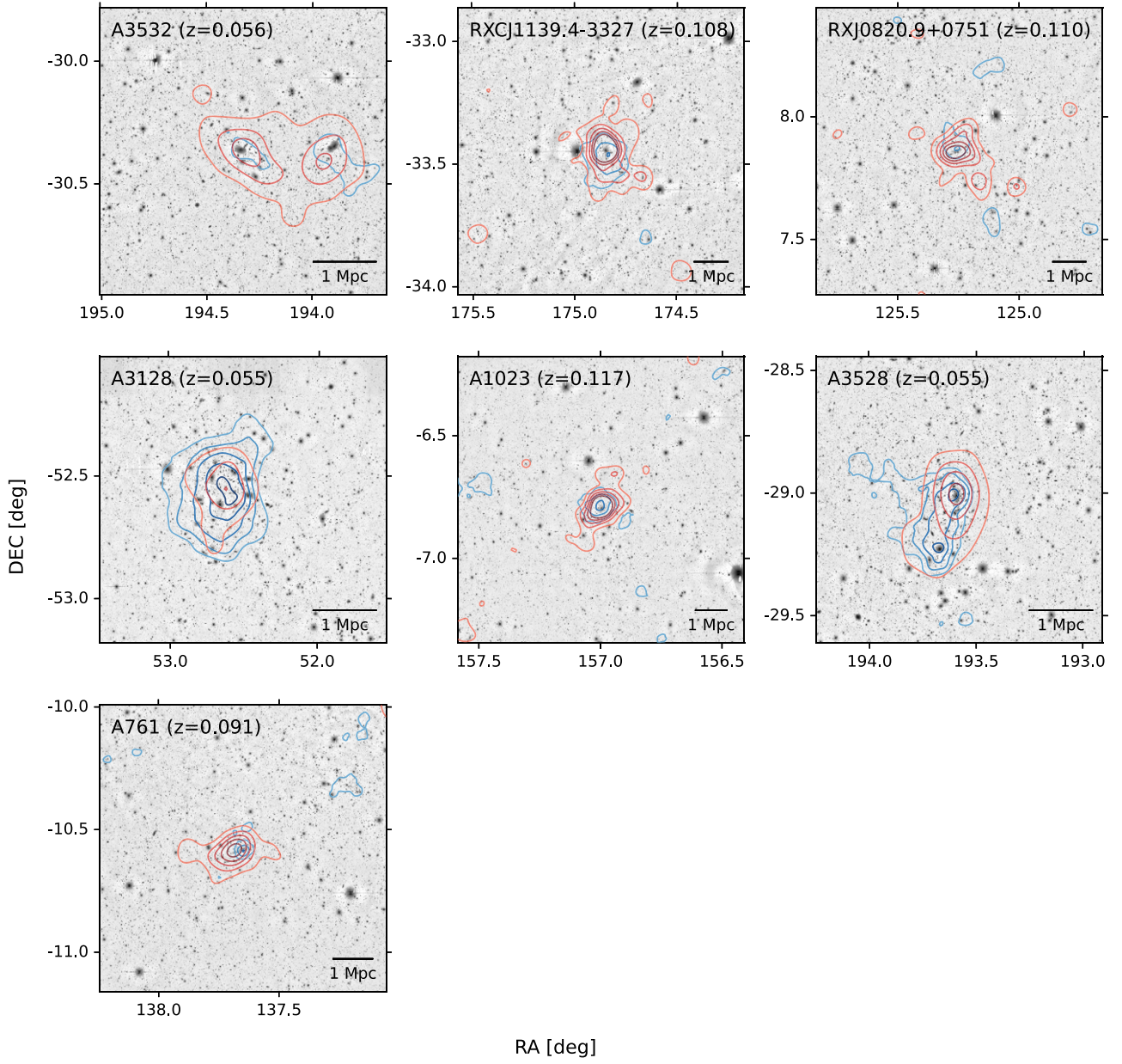


Figure 7. Grid of maps (Part V).

aperture (13k pixels; $S/N \sim 6$) before the two peaks merge into one. On the other hand, the RS distribution aligns with the orientations of two BCGs (northwest–southeast (NW–SE)).

A3667. A3667 is previously known as a merging cluster. We find that the RS galaxy distribution closely aligns (SE–NW) with the CG, which also aligns with the gas distribution and the merging direction (Knopp et al. 1996). The mass distribution shows alignment with that direction only in the cluster periphery (below 2σ) and has a large offset from that direction near the cluster center. Here, we use an aperture radius of 14k pixels when the mass S/N peak reaches a maximum (4.4σ). Our mass map is similar to the early result of Joffre et al. (2000) for the cluster central region.

A3827/A3825. We present A3827 ($z = 0.097$) and A3825 ($z = 0.074$) in the same diagram because of their proximity on the plane of sky. However, they probably are not interacting because of their large redshift difference ($\Delta z \sim 0.02$), while their RS colors could be quite similar ($\Delta(g - r) \sim 0.04$, close

to the scatter of RS). We estimate the color based on the elliptical galaxy SED template E1_B2004a used in BPZ. In the diagram, we use an aperture of 7k pixels when the A3827 S/N peak reaches a maximum (6.5σ). A3825 S/N peak reaches its maximum (2.4σ) at a small aperture of 3k pixels and is smoothed out in larger apertures. The central galaxies of A3825 are aligned with its galaxy distribution. The central strong lensing feature in A3827 has been used to test the nature of dark matter (e.g., Massey et al. 2018; Lin et al. 2023). We find a $25''$ offset between the WL S/N peak and the BCG, which is below the mass map resolution—we will further study this in the next section.

A3266. A3266 is a merging cluster. Our result shows a strong correlation between the BCG orientation and the galaxy distribution (NE–SW); the mass distribution is tilted more toward the north–south (N–S) direction, which is likely caused by a north group (instead of background clusters after visual inspection). The orientations are consistent with the merging

direction determined by galaxy motion and gas (Dehghan et al. 2017; Sanders et al. 2022). We present the first lensing map of this cluster—the mass S/N peak reaches the maximum at an aperture radius of 13k pixels (7.6σ).

A1651. A1651 exhibits similar morphology between the CG, the galaxy distribution, and the large-scale mass distribution. The mass contours extend to the west. The SW lensing peak comes from a background cluster ($z \sim 0.2$). The central mass S/N peak reaches the maximum at 12k pixels (5.1σ). Sifón et al. (2015) showed that A1651 is a relaxed cluster using spectroscopic measurements. This indicates that even nearly relaxed clusters can have elongated shapes.

A754. A754 is a merging cluster. Both the galaxy density and the mass distribution peak at the BCG, and they both align with the BCG orientation (SE–NW). Also, the galaxy density shows another peak at an SE group inside the cluster. In the mass map, a corresponding small clump is only shown in small apertures, which indicates that the substructure has a small characteristic size. The mass map peak gradually shifts to SE from NW as the aperture increases because of the SE subclump. Our mass map is similar to the early result from Subaru for the cluster central region (Okabe & Umetsu 2008). In the diagram, we use a large aperture (14k pixels) that maximizes the S/N (7.7σ).

A3571. A3571 shows alignment between the BCG, the mass distribution, and the RS galaxy distribution (N–S). These components also align with the gas distribution of this relaxed cluster (Nevalainen et al. 2000). The galaxy density value is relatively small because of the low redshift and the wide angular range. The mass NW tip likely comes from a group of member galaxies. Though we use the LSST pipeline flags to remove objects affected by saturation, here we further mask out objects within 0.25° of the SW bright star (i Cen.) to reduce artifacts, and we find that the cluster mass map does not change greatly after the cut; the residual SW clump could be caused by some background structure. We use an aperture of 11k pixels when the peak S/N reaches the maximum (3.9σ). This is the first reported WL map of the low- z cluster A3571. It is also part of the Shapley supercluster—we will present more members of this supercluster later in the text (A3558/A3532/A3528).

A3112. In A3112, the mass distribution and the galaxy distribution roughly align with the BCG along the N–S direction, and both of their peaks have small offsets from the BCG. The mass peak has an offset toward the south, which could be caused by a cluster subclump or a background cluster. The NW lobe in the RS distribution at large radii could come from a group of member galaxies; it is extending toward A3109 (NW 0.5° from A3112) and thus could be influenced by filaments inside the Horologium supercluster. We use an aperture of 11k pixels to reach the maximum 4.4σ in the mass map. This is the first high-resolution lensing map of A3112.

A2597. A2597 shows a weaker lensing signal compared to the clusters that have similar X-ray luminosities. We choose the aperture at 5k pixels to show an S/N maximum (3.3σ). The galaxy distribution aligns with the BCG at small radii (SE–NW) and tilts more to the N–S direction at large radii due to a group of member galaxies.

A1650. A1650 (SDSS-C41041) shows the orientation alignment between the BCG, the mass distribution and the RS galaxy distribution. The east mass clump could come from a background cluster/group. For the mass map, we use an aperture of 14k pixels that maximizes the peak S/N (4.9σ).

A3558. A3558 lies at the center of the Shapley supercluster. In the diagram we present A3558 (center; $z = 0.047$) and its neighboring clusters A3562 (east; $z = 0.049$) and A3556 (west; $z = 0.048$). We find alignment between the CG, the mass distribution, and the galaxy distribution of A3558. Both the mass distribution and the galaxy distribution peak at the BCG of A3558 and extend SE toward A3562—in between, we notice low-mass S/N detection ($\sim 1\sigma$) and a low-density stream of bright RS galaxies (~ 0.015 per 100×100 pixels; $\sim 25 \text{ Mpc}^{-2}$), which indicates filaments connecting A3558, A3562, and the central groups between the two. On the other hand, we find no clear signal between A3558 and A3556 in both mass and galaxy distributions. Here, we use an aperture of 12k pixels that maximizes the S/N (5.0σ), and we show the central 11×5 patches ($44\text{k} \times 20\text{k}$ pixels; $3.2^\circ \times 1.5^\circ$) to include all three clusters. The mass and galaxy distributions are consistent with the gas distribution (Planck Collaboration et al. 2014) and are similar to the previous results of Higuchi et al. (2020), and our depth is ~ 1.5 mag deeper.

A3695. We find alignment in orientations between the BCG, the galaxy distribution, and the mass distribution of A3695 at small radii, though these distributions show distorted shapes at large radii, which could be caused by merging. The CG has two peaks (showing a “dumbbell” shape) along its major axis, indicating a possible merging direction (NW–SE). We use the mass map that has the highest S/N peak (4.9σ) at an aperture of 6k pixels.

A3921. A3921 is a merging cluster and has been studied via WL in Paper I. Here, we use a higher photo- z cut and obtain a similar mass map. We adopt an aperture of 11k pixels that maximizes the S/N (3.3σ). Also, we include an RS map, which has two peaks—one corresponds to the BCG (SE) and the other corresponds to a group (NW). These peaks also match the main and secondary components of the merging cluster.

A2426. A2426 shows alignment between the orientations of the BCG and the RS galaxy distribution (east–west (E–W)), while the mass distribution is along the N–S direction. There may be an infalling group in the NW corner of the cluster, which would explain the mass distribution elongation. The mass concentration in the SE of the diagram is likely caused by a background cluster/group. The RS clumps at the NE corner of the diagram may come from a nearby/foreground group. For the mass map, we use an aperture of 10k pixels when the peak S/N reaches a maximum (4.2σ).

A3158. A3158 is a merging cluster as suggested by its X-ray emission and member galaxy motions (Whelan et al. 2022). Similarly, the CG shows two strong peaks, which also align with the galaxy and gas distributions (NW–SE). The mass distribution tilts more to the N–S direction near the cluster center. This is the first high-resolution WL map of A3158—here, we use an aperture of 11k pixels that maximizes the S/N (6.7σ). A3158 is in the Horologium supercluster close to A3128 (presented later; 2.2° away). After combining their catalogs, we find no clear sign of filaments between the two clusters except for some isolated groups.

RXCJ1217.6+0339. The mass and galaxy distributions and the CG of RXCJ1217.6+0339 (RBS1092/ZwCl1215+0400) show the orientation alignment (NE–SW), and the offsets between their peaks are small. We use an aperture of 7k pixels that maximizes the peak S/N (6.0σ).

A2811. In A2811 the mass distribution orientation weakly aligns with the CG (NW–SE). The galaxy distribution roughly

aligns with the E–W direction at small radii and aligns with the CG at large radii. The peak S/N reaches the maximum (5.3σ) at an aperture of 6k pixels as shown in the mass map. The galaxy overdensity at the SW corner of the diagram comes from A2804 but without a clear lensing signal, which is likely caused by its low mass inferred from the X-ray emission (Obayashi et al. 1998; Sato et al. 2010).

A780. A780 (Hydra A) shows alignment between the orientations of the BCG and the galaxy distribution (NW–SE); the RS galaxies extend more toward SE due to an infalling group (around LEDA87445; ~ 1 Mpc SE of the cluster center), which is consistent with previous studies on the X-ray and spectroscopic data (Girardi et al. 2022). The mass distribution is approximately along the E–W direction at small radii. Here, we use an aperture of 6k pixels that reaches an S/N maximum of 4.0σ .

A2420. The BCG and the galaxy distribution at small radii have similar orientations (NE–SW); at large radii, the galaxy distribution is more disturbed due to nearby groups. The mass distribution extends in the E–W direction generally; we use an aperture of 7k pixels where the S/N reaches the maximum of 4.9σ .

A1285. The BCG(s) of A1285 is an interacting pair aligning with the NW–SE direction. The mass and RS galaxy distributions also generally align in that direction. Both the mass and RS maps indicate a nearby group to the east of the cluster, and there could be a few infalling groups on the periphery of the cluster suggested by the galaxy distribution. For the mass map, we use an aperture of 12k pixels when the peak S/N is maximized at 6.1σ . After mass fitting, we note that A1285 seems to have a higher mass compared to clusters that have similar X-ray luminosities.

A3911. A3911 has been analyzed via WL in Paper I. We further include the RS galaxy distribution in this paper, which aligns with the BCG along the NW–SE direction. The BCG shows signs of interaction and has two cores. The lensing mass map is similar to the result in Paper I, after a higher photo- z cut on the source galaxies implemented in this work. Here, we use an aperture of 10k pixels that maximizes the peak S/N at 4.9σ . The galaxy group at the north edge of the diagram may be related to a nearby cluster A3915 ($z = 0.096$; $\sim 0.7^\circ$ from A3911).

A2055. A2055 has no sign of a giant BCG but a group of bright ellipticals concentrating at the cluster center and several RS galaxies spreading along the NW–SE direction. The mass map shows a complex shape surrounding the central galaxies, and the peak has a clear offset from those central galaxies, which might indicate that the cluster is undergoing merger activity. We use an aperture of 8k pixels—the mass S/N map peak reaches a maximum of 3.1σ , which is much lower than the clusters that have similar X-ray luminosities and redshifts (and leads to a low lensing mass).

A1750. A1750 is a merging cluster that has three subclusters located at the north (A1750N), center (A1750C), and south (A1750S). The galaxy distribution shows peaks located at the BCG of each subcluster. The RS galaxy density has the highest peak at A1750C, which is also true for the X-ray surface brightness (Bulbul et al. 2016). Note there is another galaxy density peak at the SW corner of the diagram corresponding to a nearby cluster—SDSS-C41191 ($z = 0.087$; likely low mass). For the mass map, under a small aperture (≤ 5 k pixels) the peak is at A1750C ($\leq 4.5\sigma$), but under a large aperture (≥ 6 k pixels)

the peak is at A1750N. This suggests that A1750C has a smaller characteristic size than A1750N, but we also note a background cluster XCLASS468 ($z = 0.56$) $\sim 3'$ SW of A1750N, which could partially contribute to the lensing signal around A1750N. In the diagram, we use an aperture of 10k pixels when the S/N is at a maximum of 5.4σ to show the cluster-scale structure. A1750S has no clear lensing signal (maximum 0.4σ at a small aperture of 4k pixels), and it produces weak X-ray emission as well (Bulbul et al. 2016). The clump to the east of A1750 could come from a background compact group SDSS-CGB7175. Our results are similar to the previous Subaru study (Okabe & Umetsu 2008), but we use a larger FoV and thus are able to show the structure around A1750.

A3822. A3822 has two close BCGs and a few bright galaxies at the cluster center. There is another BCG in the NE, and the mass and RS galaxy distributions extend toward that direction (similar phenomenon has been found in the X-ray emission; Lakhchaura & Singh 2014), indicating a possible cluster merger. The central BCGs align along the NE–SW direction as well. However, near the cluster center the orientations of mass and RS distributions align more with the E–W direction. In addition, there are signs of groups in the NW connecting A3822 with a neighboring cluster A3806 ($z = 0.075$; $\sim 1.1^\circ$ from A3822). For the mass map, we use an aperture of 12k pixels where the S/N peak reaches the maximum (6.3σ). This is the first reported lensing result of A3822.

A2941. The BCG(s) of A2941 has multiple cores showing signs of merging. The RS distribution aligns with the BCG (E–W). The mass distribution near the center is along the N–S direction and tilts more toward the NE–SW direction at large radii. For the mass map, we use an aperture of 9k pixels where the peak S/N reaches the maximum (4.4σ). This is the first published lensing result of A2941.

A2440. A2440 is a merging cluster that shows a chain of bright elliptical galaxies along the NE–SW direction without a clear sign of a single BCG. Nonetheless, the orientations of those bright ellipticals seem to align with the RS galaxy distribution, which is consistent with previous studies (Maurogordato et al. 2011) and we use a larger FoV. The mass S/N map shows a complex shape—at small radii, the mass distribution is roughly along the NW–SE direction. We tested further masking a circular region with a radius of 0.05° around the northern bright star (HD212427; within the mass contour) and found no significant change on the mass map. A mass clump near the west edge of the diagram could come from a background cluster (RMJ222223.6-014423.7). Here, we use an aperture of 7k pixels where the peak S/N reaches a maximum of 4.1σ .

A1644. A1644 is a merging cluster. The RS galaxy distribution shows two peaks—a strong peak (A1644N) in the north corresponding to a group, and a weaker peak (A1644S) near the BCG. The mass distribution peaks at the BCG and extends to the south. In the mass map, we use an aperture of 13k pixels where the peak S/N reaches the maximum (6.2σ). We note that under small apertures, there is a small mass peak ($\sim 2\sigma$ at an aperture of 3k pixels) near the northern group, but it could be caused by shape noise as well. The RS galaxy distribution approximately aligns with the mass distribution (the N–S direction). Our results are similar to the

ones of Monteiro-Oliveira et al. (2020), and we use deeper data and a different pipeline.

A1348. A1348 shows alignment between the orientations of the BCG, the mass, and galaxy distributions at small radii; both distributions extend to the south at large radii. The RS density peak shows a small offset from the BCG. The galaxy distribution has a complex shape at large radii, which could partially be caused by the infalling of neighboring groups, or projection effects of the nearby structure along the line of sight due to the RS scatter; a more detailed study requires sufficient spectroscopic redshift measurements. A foreground bright elliptical galaxy to the SW (2MASX J11405929-1223536; $z = 0.074$) and its neighboring galaxies could contaminate the RS distribution because of similar colors. For the mass map, we use an aperture of 6k pixels that gives the maximal S/N (4.8σ).

RBS1847. In RBS1847 (2MAXI J2216-647) the CG orientation is quite different from the RS and mass distributions. The single BCG is generally along the E-W direction. The mass distribution is along the NW-SE direction (at small radii), while the galaxy distribution is along the NE-SW direction. The misalignment between the three might be related to the cluster's dynamical history. We use an aperture of 10k pixels where the S/N peak reaches the maximum (4.2σ). This is the first lensing mass map of RBS1847.

RXCJ1215.4-3900. In RXCJ1215.4-3900, the BCG mostly aligns with the E-W direction and is slightly tilted NE-SW. However, the cluster shows alignment between the mass and galaxy distributions at large radii along the N-S direction, and the RS distribution shows a southern group that could be infalling. We use an aperture of 9k pixels where the S/N reaches the maximum (4.8σ). This is the first lensing mass map of RXCJ1215.4-3900.

A2351. A2351 exhibits alignment between the orientations of the BCG, the mass, and galaxy distributions (NW-SE), especially near the cluster center. The BCG has a dumbbell shape showing signs of interaction. We tested the effect of adding masks (radius 0.05°) around the central bright stars (V* AS Cap. and HD205131) near the BCG, but this did not change the mass map greatly. Here, we use an aperture of 8k pixels where the S/N reaches a maximum of 4.0σ . This is the first lensing mass map of A2351.

RXCJ2218.2-0350—RXCJ2218.2-0350 is a merging cluster. Near the cluster center there is a stream of bright ellipticals, and their orientations are generally aligned with the galaxy and mass distributions (NE-SW). RXCJ2218.2-0350 can be divided into two subclusters at NE and SW, respectively. The X-ray (Gu et al. 2019) and RS peaks are both at the NE subcluster, but the mass map peak is at the SW subcluster, which may have been affected by merging. A few nearby groups/clusters (with low masses) are also shown in the RS galaxy distribution. We show the mass map with an aperture of 5k pixels when the peak S/N is maximized at 3.8σ . This is the first mass map of RXCJ2218.2-0350.

A2443. A2443 is a merging cluster. We find that the galaxy distribution is along the NW-SE direction, which is consistent with the gas (Clarke et al. 2013) and previous studies (Golovich et al. 2019). The mass distribution is oriented N-S and peaks at the BCG, while the RS density peak shifts to the north. We use an aperture of 5k pixels that maximizes the S/N peak (6.2σ) of the mass map in the diagram.

A2050. A2050 shows alignment between the orientations of the BCG, the galaxy distribution, and (at small radii) the mass

distribution along the NE-SW direction, and the distributions stretch more to the south at large radii. We show the mass map at an aperture of 4k pixels that maximizes the S/N peak at 4.0σ .

A1736. A1736 has multiple BCGs (e.g., IC4252, ESO509-8, ESO509-9; separated by ~ 0.7 Mpc). The CG ESO509-9 has a close and bright companion LEDA47075, and several bright ellipticals are scattered ~ 0.5 –1 Mpc from the cluster center, suggesting that A1736 is undergoing a merger. The RS distribution aligns with the central BCG orientation (N-S) at small radii, while the mass distribution shows the alignment approximately at large radii. The mass distribution is along the NE-SW direction at small radii, and the mass peak lies to the NE ($\sim 2' \sim 0.1$ Mpc) of the CG. In the mass map, we use an aperture of 11k pixels that maximizes the S/N peak at 3.9σ . This is the first reported WL mass map of A1736.

A2384. A2384 is a merging cluster. RXCJ2152.2-1942/A2384(B) is in the SW (~ 1 Mpc) of A2384. The BCGs of both (sub-)clusters generally align with the orientations of their combined mass and galaxy distributions (NE-SW) and the gas as well (Parekh et al. 2020). Each cluster has an RS density peak—A2384 has higher density, and the density drops and rises along the line from A2384 to A2384(B), indicating the filaments connecting the two clusters (consistent with Maurogordato et al. 2011). The mass map peak is close to the BCG of A2384. In the diagram, we use an aperture of 7k pixels that maximizes the S/N peak of the mass map at 5.7σ .

A4059. A4059 has low (angular) surface density in mass and galaxy number due to its low redshift; the lensing signal is further decreased by its high critical surface density at low redshift, which leads to low aperture mass S/N. Despite that, A4059 shows the alignment between the orientations of the BCG, the RS galaxy distribution, and roughly the mass distribution (NW-SE), and the gas distribution also has a similar orientation at large radii (Bartolini et al. 2022). The mass peak is slightly shifted to the SW of the BCG, which could be affected by shape noise because of the low lensing signal, but we note that there is a concentration of gas in the SW of the BCG as well. In the diagram, we show a mass map using an aperture of 5k pixels that maximizes the peak S/N at 2.8σ . This is the first WL map of A4059.

A3836. In A3836, the RS distribution aligns with the BCG orientation (N-S), while the mass distribution extends along the E-W direction. In the mass map, we use an aperture of 8k pixels when the S/N peak reaches a maximum (4.9σ). This is the first reported lensing map of A3836. Near the diagram SW corner, the mass and RS peaks may correspond to a nearby cluster Ser148-4.

A2533. A2533 exhibits alignment between the orientations of the BCG and the RS galaxy distribution at small radii (NE-SW); at large radii, the galaxy distribution is more tilted to the N-S direction. The mass distribution is along the NW-SE direction; the peak is slightly shifted to the east. We use an aperture of 8k pixels that maximizes the S/N peak at 4.6σ . This is the first lensing mass map of A2533.

A2556/A2554. In the diagram, we present A2556 (east; $z = 0.087$) and A2554 (north; $z = 0.109$), together with A2550 (middle south; $z = 0.123$), which all show concentrations of RS galaxies. The lensing signal and concentration of RS galaxies at the bottom of the diagram come from A2555 (south; $z = 0.111$). Similar to A3827/A3825, A2554/A2556 likely have no interaction because of their redshift difference

($\Delta z \sim 0.02$), but their RS colors are similar ($\Delta(g - r) \sim 0.04$), and A2556 has no significant lensing signal (maximum $\sim 2.8\sigma$ at an aperture of 3k pixels; smaller at larger apertures). Likewise, A2550 does not show a clear lensing signal (maximum $\sim 2.5\sigma$ at an aperture of 3k pixels), and its color difference compared to A2556 is also small ($\Delta(g - r) \sim 0.06$). A2554 shows the alignment between the orientations of the BCG and the RS distribution (N–S), but the mass distribution aligns with the E–W direction generally. The RS distribution also aligns with the gas distribution, and the X-ray and spectroscopic observations indicate that A2554 is a perturbed system (Erdim & Hudaverdi 2019). For A2556 we find the directions of the BCG and the RS distribution approximately align. In the diagram, we use an aperture of 6k pixels where the peak S/N of A2554 reaches the maximum (4.5σ), but A2556 and A2550 are at $\sim 1.7\sigma$, indicating their small characteristic sizes.

A3126. In A3126, both the galaxy and mass distributions show circular shapes at small radii, and the BCG is nearly circular as well (but shows signs of merging with a member galaxy at NW). At large radii, the galaxy distribution stretches along the NW–SE direction, while the mass distribution extends in the N–S direction. On the mass map, we also notice clumps in the north, SE, and SW of A3126, and they are shown in the DES Y3 mass map as well (Jeffrey et al. 2021); these clumps could come from nearby/background groups. We use an aperture of 6k pixels where the peak S/N reaches a maximum at 4.7σ .

RXCJ0049.4–2931. RXCJ0049.4–2931 (ACOS84) shows the orientation alignment between the BCG and the mass distribution (SE–NW), while the RS distribution is generally along the N–S direction. In the mass map, we use an aperture of 6k pixels when the S/N peak reaches a maximum at 4.2σ . This is the first lensing mass map of RXCJ0049.4–2931.

A3395. A3395 is a merging cluster and has two components (A3395N and A3395S), each with a BCG (ESO161-8 and LEDA19057, respectively). The lensing peak is close to the southern BCG, and A3395S produces stronger X-ray emission than A3395N (e.g., Reiprich et al. 2021). The RS peak is near the northern BCG, which is also brighter and larger than the southern BCG. The RS distribution and the northern BCG present similar orientations. We use an aperture of 10k pixels for the mass map, where the S/N peak reaches the maximum (4.4σ). This is the first reported WL map of A3395.

A1606. A1606 has been studied by McCleary et al. (2020) via WL. Here we reanalyze it using deeper data (~ 2 mag) and present the RS map as well. The orientations of the RS distribution and the BCG are roughly aligned. In the mass map, we use an aperture of 6k pixels where the S/N peak reaches the maximum 3.9σ .

A2670. In A2670, the BCG and the mass and galaxy distributions at small radii are nearly circular. At large radii, the mass distribution is roughly along the NW–SE direction and the RS distribution is generally along the N–S direction. In the diagram, we show the mass map using an aperture of 10k pixels that maximizes the peak S/N at 5.8σ .

A3532. A3532 has a close companion A3530 that is below our X-ray luminosity cut (west of A3532 in the diagram). The two clusters may just start to interact (Lakhchaura et al. 2013). We note that under small apertures A3532 has a higher aperture mass S/N than A3530, while under large apertures it is the opposite. Therefore, we use an aperture of 8k pixels so that

both peaks have close S/N (~ 3) to show the structure in both clusters. This is the first WL mass map of A3532. A3532 has a higher RS density than A3530, and both clusters show orientation alignment between the BCG and the RS distribution. A3532 also shows alignment between the BCG and the mass distribution. The BCGs of both clusters have dumbbell shapes showing signs of merging.

RXCJ1139.4–3327. In RXCJ1139.4–3327, we find that the CG has two cores, which are both nearly circular near the center, but their merged galaxy envelope extending to the ICL is along the N–S direction. Interestingly, both the lensing mass and RS galaxies are generally distributed along the N–S direction as well. The distribution peaks are slightly shifted from the BCG, which could be physical or caused by noise. In the mass map, we use an aperture of 8k pixels when the peak S/N reaches the maximum at 4.0σ . This is the first lensing mass map of RXCJ1139.4–3327.

RXJ0820.9+0751. In RXJ0820.9+0751 (RXJ0821.0+0752), we find that the BCG and both the mass and galaxy distributions at small radii are along the NW–SE direction. At large radii, both distributions are more disturbed—there is a group of RS galaxies to the south of the cluster (~ 1 Mpc within the lowest contour of the cluster), which could be an infalling group. Another RS density peak to the SW of the cluster ($\sim 0.3^\circ$) could come from a foreground group. For the mass map, we use an aperture of 8k pixels where the peak S/N reaches a maximum at 3.1σ . This is the first reported WL mass map of RXJ0820.9+0751.

A3128. A3128 is a merging cluster in the Holograms supercluster (see also the paragraph for A3158 above). There are a few bright ellipticals at the cluster center showing different orientations, and in the NE of the cluster (~ 0.5 Mpc) there is a massive background cluster ACT-CLJ0330-5227/DESJ0330-5228 ($z = 0.44$; $M_{200c} \sim 10^{15} M_\odot$; McCleary et al. 2015; Nord et al. 2016) which can contribute to the lensing signal, and thus we mask the background sources within r_{200c} of the background cluster. The final mass map has two central peaks at NE and SW, respectively (separated by $\sim 4' \sim 0.3$ Mpc), which is similar to the previous lensing result of McCleary et al. (2015), and we use deeper data (by ~ 1 mag in the u , g , z bands) and include i , Y bands for photo-z measurements. We find that at large radii the mass and galaxy distributions are both approximately aligned with the N–S direction. Here, we use an aperture of 11k pixels where the mass map S/N peak reaches the maximum at 6.2σ . Interestingly, the two mass map peaks roughly match the X-ray emission peaks of A3128 (after removing the background cluster emission; Werner et al. 2007).

A1023. In A1023, the BCG orientation generally aligns with the galaxy distribution (NW–SE); the mass distribution aligns with that direction only at small radii, and is more circular at large radii. The mass peak at the NW corner of the diagram comes from a background cluster A1013. We use an aperture of 5k pixels that maximizes the peak S/N at 4.4σ . This is the first mass map of A1023.

A3528. A3528 is a merging cluster that has two BCGs separated by ~ 1 Mpc at NW and SE, corresponding to two subclusters, A3528N and A3528S. The RS galaxies gather near the northern BCG (ESO443-4) and their distribution aligns with the orientation of the northern BCG at small radii (the N–S direction); at large radii, the galaxy distribution extends to SE and spreads out around the southern BCG (ESO443-7). The gas

distribution orientation also aligns with the BCGs (Gastaldello et al. 2003). The mass map shows two central peaks corresponding to the two BCGs under small apertures. When the aperture expands, the mass S/N map peak reaches a local maximum of 5.0σ at an aperture of 4k pixels; after that, the peak S/N keeps increasing as the aperture expands because of the large separation between the two central clumps, and the corresponding northern and southern peaks start to merge into one central peak at an aperture of 8k pixels. In the diagram, we thus use an aperture of 7k pixels to show the two peaks. In addition, the NE clump in the mass map probably comes from a background cluster SPT-CLJ1256-2851 ($z = 0.36$), but we expect that its contribution to the A3528 central lensing signal is small because of the large angular separation between the two clusters. The mass clump at the bottom of the diagram could come from nearby/background groups. This is the first reported lensing mass distribution of A3528.

A761. In A761, the mass map peak is close to the BCG (PMNJ0910-1034), but the RS distribution is slightly offset to the east (its peak is close to another bright CG LEDA976301). We use an aperture of 4k pixels for the mass map, where the S/N peak reaches the maximum (4.1σ). This is the first WL map of A761. The RS distribution shows alignment with the BCG orientation.

4.2. Orientation Alignment between the Mass and Galaxy Distributions and the BCG

The figures in Section 4.1 show striking similarities between the orientations of the mass/RS distributions and the BCG, especially between the RS distribution and the BCG, in individual clusters. Therefore, we use the method described in Section 3.5 to quantify their orientation angles, and then we study the difference between those angles as a function of cluster dynamical state and radial distance range (Figure 8). When computing the difference angle, we use its supplementary angle if it is larger than 90° . Because it is difficult to determine the cluster dynamical state without enough spec-z data, we instead use the number of central galaxies (number of CG = 1, 2, or ≥ 3) as a proxy—clusters with more bright central galaxies tend to be more perturbed (Edwards & Patton 2012; Mann & Ebeling 2012; Furnell et al. 2018). We require that the central galaxies being counted are sufficiently larger and brighter than other member galaxies and clearly separate from neighboring large member galaxies. In the future, we will also seek to use the X-ray/SZ information to determine the cluster's dynamical state.

In Figure 8, we find that, statistically, the RS galaxy distribution aligns with the BCG orientation throughout the entire cluster region and the alignment even extends to LSS, while the mass distribution and the RS galaxy distribution show alignment between their orientations only inside the cluster with a larger offset angle, and the mass distribution and the BCG align only near the cluster center. This is similar to the results of Oguri et al. (2010) and Chu et al. (2021), but their samples are in different redshift ranges than ours and are studied using different instruments and methodologies. Also, we note that all types of alignment seem not to strongly depend on the cluster redshift and the dynamical state, however this observation could be limited by the cluster sample size. The “significance” of the orientation alignment can be estimated by Monte Carlo tests or analytically calculated by the cumulative function of a binomial distribution (Appendix F). We find that

the probability of more than half of the cluster sample having an angle difference below 30° is $\sim 0.5\%$, which is significantly small, assuming the angle difference is uniformly distributed between 0° and 90° . It indicates that only random fluctuation can not account for the large number of cases where the angle between the RS distribution and the BCG/mass distribution (within 1 Mpc) is below 30° .

The strong alignment between the orientations of the BCG and the RS distribution may result from the long-term dynamical process that those low-z massive clusters have undergone. The RS galaxies we have selected are relatively bright, and therefore, they are older and have remained in the cluster longer than other members. The CG and the RS galaxy distribution tend to align because of the gravitational potential (Donahue et al. 2016) or more specifically the filamentary accretion and the tidal field (Huang et al. 2016). The cluster dwarf members and blue members can also affect the galaxy distribution morphology, but their membership is difficult to determine without spectroscopic data. For lensing mass distributions, shape noise affects their orientations randomly. Thus, the effect of shape noise is statistically reduced in a large cluster sample (like the sample in this work) for deriving the median misalignment, and the larger sample size helps bolster confidence in our results—we will revisit this analysis for the whole LoVoCCS sample. Additionally, it is worth pointing out that previous studies mostly focus on the clusters at higher redshift ($z > 0.1$) which generally experience shorter evolution time than this sample.

4.3. Distribution of Center Offset

The figures in Section 4.1 also show a rough consistency between the peaks of the maps and the BCG position. Here, we compare those positions by studying their distances and relative position angles. The positions are measured by the method in Section 3.5, and we convert their angular separations into physical ones to simplify comparison.

The result is presented in Figure 9. We find that most positions are aligned (median ~ 0.1 Mpc), but perturbed clusters tend to have larger separations. Also, the position difference has no clear dependence on the position angle, suggesting no significant systematics. The distance distribution is similar to previous results (e.g., Oguri et al. 2010; von der Linden et al. 2014; Donahue et al. 2016).

We note that mass maps could be affected by background clusters, and RS maps could be affected by photometry noise or nearby groups/LSS. However, when we combine the results from a sample of clusters (as in this work), we can treat the locations of interlopers as random, so that they contribute to noise without systematic bias at the peak location.

As the offset between the mass center and the BCG in relaxed clusters (the BCG “wobbling”) may indicate SIDM, we further discuss the result in Section 5.3.

5. Discussion

5.1. Shape Correlation, PSF Modeling, and Shape Measurement

As mentioned in Section 3.6, we use TreeCorr to compute shape correlations—the cross-correlation between the shapes of stars and galaxies, and the autocorrelation of stellar shapes. We use those correlations to estimate the PSF modeling bias in the lensing shear measurements. The details are given below.

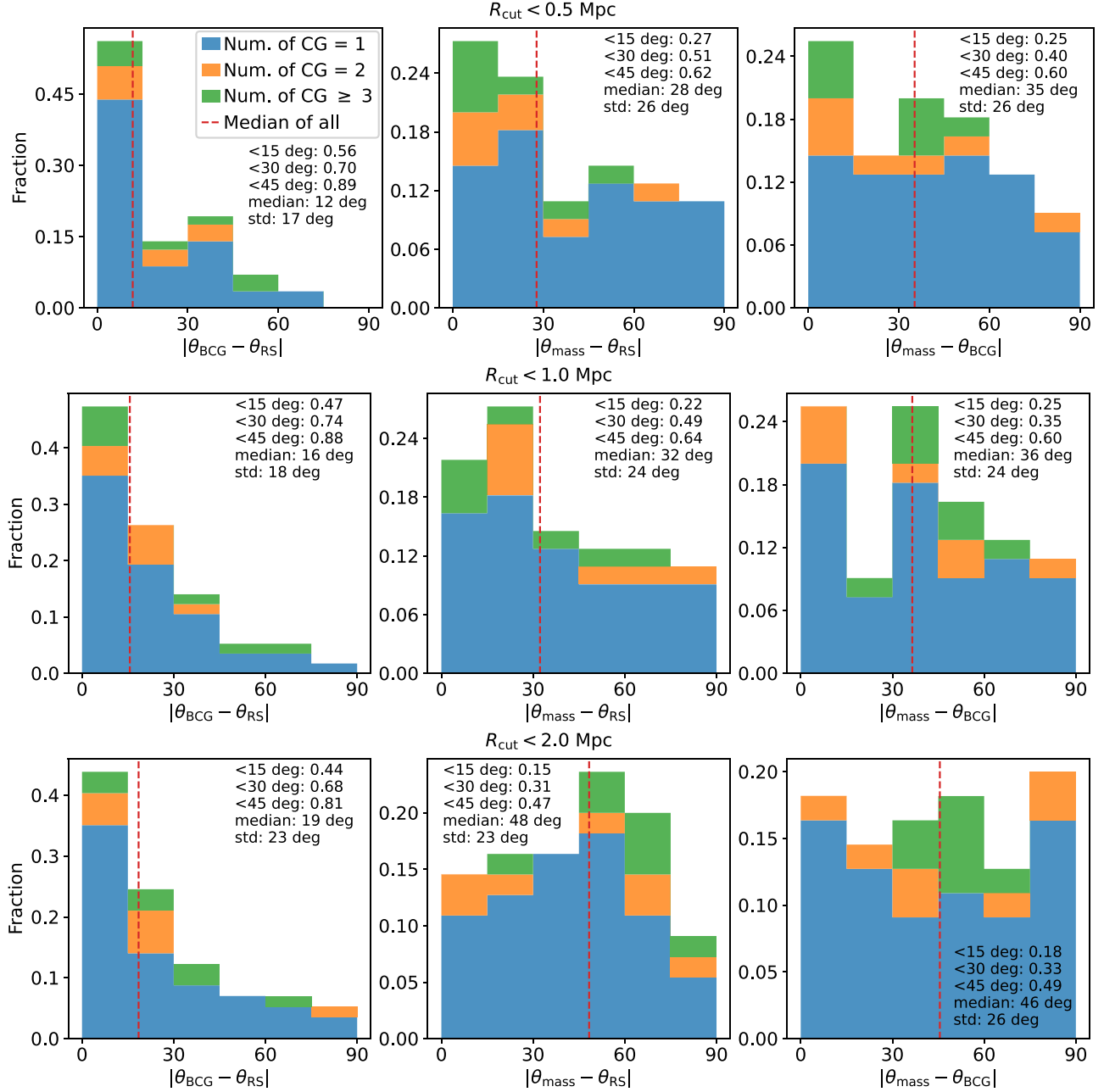


Figure 8. Orientation alignment between the BCG, the RS galaxy distribution, and the lensing mass distribution in each cluster of our sample. The histograms are stacked on top of each other. We consider the distributions within radial distance cuts of 0.5, 1.0, and 2.0 Mpc, respectively. The Y-axis shows the fraction in the sample (the total fraction is 1). We give the fractions within 15° , 30° , and 45° in the text box, together with the median (the vertical dashed line) and the standard deviation of all clusters. The angles are in degrees.

We consider the correlations in Equations (4) and (5), where the superscripts α, β are star (s) or galaxy (g), the subscripts i, j are 1 or 2, $e_i(\mathbf{R})$ is the i th component of the ellipticity/shape of an object at coordinate \mathbf{R} , \mathbf{r} is a vector with length r connecting two objects, and $\hat{\mathbf{r}}$ is the unit vector of \mathbf{r} .

$$C_{ij}^{\alpha\beta}(r) = \langle e_i^\alpha(\mathbf{R}) \cdot e_j^\beta(\mathbf{R} + \mathbf{r}) \rangle_{\mathbf{R}, \hat{\mathbf{r}}} \quad (4)$$

$$C^{\alpha\beta}(r) = C_{11}^{\alpha\beta}(r) + C_{22}^{\alpha\beta}(r). \quad (5)$$

To compute the correlations, we use the stars for PSF modeling in the central 6×6 patches, and we use their SDSS shapes derived from second moments without PSF correction. For galaxies, we use the high-quality selection from lensing analysis and utilize their PSF-corrected HSM shapes

(Section 3.3; r -band depth ~ 26 mag). The measured galaxy shape can be described as a sum of three elements (in the first order expansion)—the intrinsic shape (shape noise), the WL-induced distortion (proportional to shear), and the PSF residual (the PSF “leakage”). After cross correlating the galaxy shapes with the star shapes (equivalent to the PSF), we expect that the contributions from shape noise and lensing in the galaxy shapes should be averaged out, as they are random to PSF. If we assume that the PSF residual is proportional to the PSF, then the proportionality factor can be estimated by the ratio between the galaxy-star and star-star correlations (C^{sg}/C^{ss}). Here, we consider the contributions from the 1–1 and 2–2 component correlations; our test shows that the contributions from the 1–2 and 2–1 correlations are smaller. Next, we can obtain an

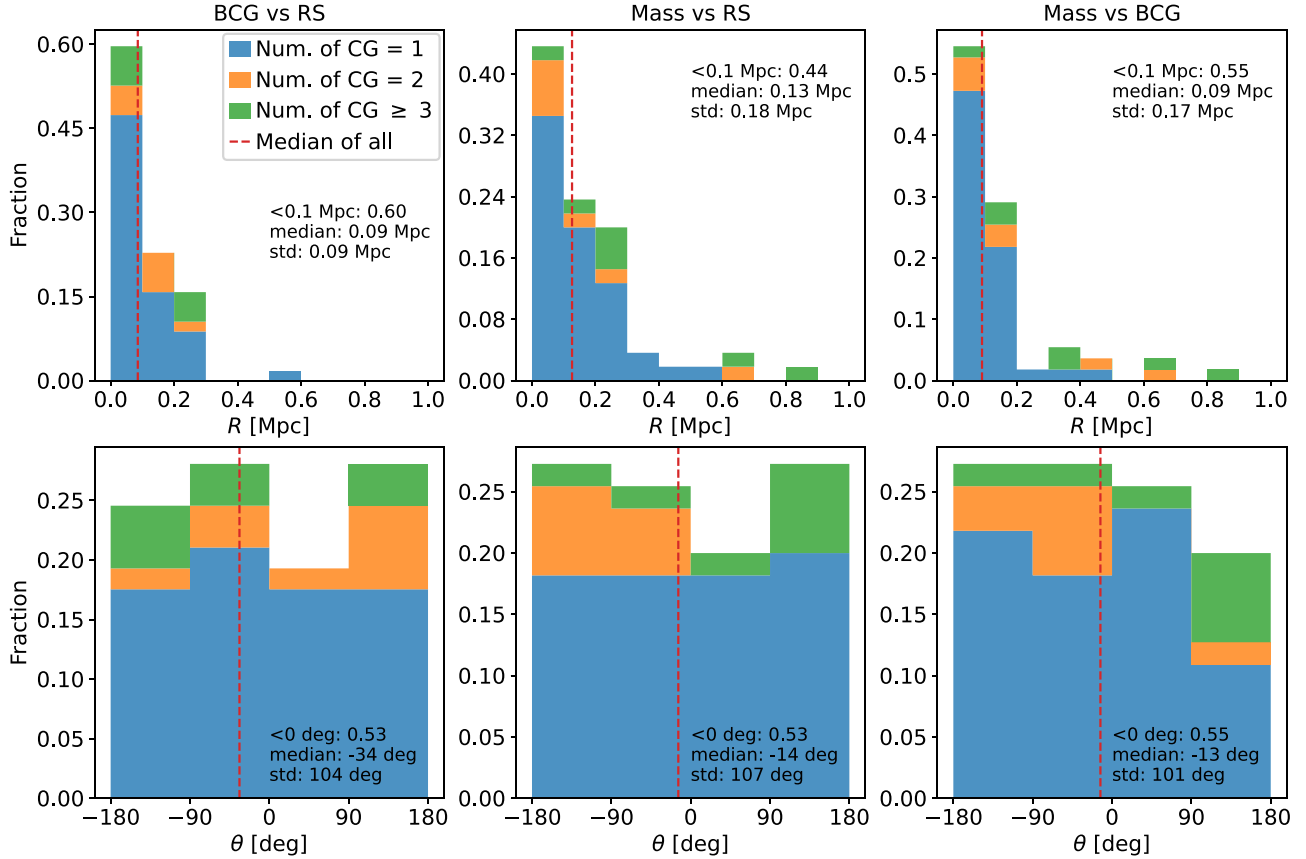


Figure 9. Offsets between the centers of the BCG, the RS distribution, and the mass distribution in each cluster of our sample. The top panel shows the distance distribution, while the bottom panel shows the (relative azimuth) angle distribution. Similar to Figure 8, the histograms are stacked for visualization, and the vertical dashed line gives the median of all clusters in the sample. For reference, the standard deviation of a uniform distribution is $\sim 29\%$ of the range (here $\sim 104^\circ$).

estimate of the PSF shape magnitude from the star-star correlation ($\sqrt{C^{ss}}$), and thereby estimate the magnitude of the PSF residual by $C^{sg}/\sqrt{C^{ss}}$. Note that the term must be divided by 2 when compared to the (reduced) shear g since $g_i \sim \langle e_i \rangle / (2\mathcal{R})$ in WL, and the typical shear responsivity \mathcal{R} is $\sim 1/1.2$ (Paper I) and can be treated as a secondary factor here. Similar methods have been used in the studies of Jarvis et al. (2016) and Mandelbaum et al. (2018b).

Figure 10 shows that the effect of PSF modeling bias on the shear measurement—the $C^{sg}/(2\sqrt{C^{ss}})$ ratio—is at the level of $\sim 10^{-3}$. We tested and found that using the calibrated per-object shear estimate instead can produce a similar result. Since the typical shear value in the cluster region that we are interested in is ~ 0.02 (at $\sim 0.5r_{200c}$ for representative NFW halos; Section 5.3), we conclude that the PSF modeling bias on shear measurements is $\lesssim 10\%$ (at percent level on average). We also note that the clusters with larger ratio values usually have larger masses, and thus their lensing shear signals are also larger, which compensates for the higher biases.

5.2. Mass Map

Some LoVoCCS clusters are covered by DES, and we compare our mass maps with the recent DES Y3 WL mass maps (Jeffrey et al. 2021). We select the Wiener map from the DES Y3 maps, which has the best performance among the methods used in that study. The Wiener map maximizes the convergence posterior using a Gaussian prior and gives a better reconstruction of mass distribution for LSS than clusters. While

the DES Y3 maps used sources from different redshift bins, we use the full redshift range that includes all galaxies at different redshifts since our clusters are at very low redshift $z \lesssim 0.1$. Although the DES Y3 maps are posterior convergence maps instead of aperture mass maps (as in this work), we expect the mass distribution morphologies described by the two types of maps to be consistent (Sections 3.2 and 3.3). After comparison, we find that in those cluster fields our maps are similar to the DES Y3 maps, and that our maps have higher resolution resulting from depth.

5.3. Mass-BCG Center Offset

Following Section 4.3, here we further discuss the centroid offset between the lensing mass distribution and the BCG in relaxed clusters as a possible tracer of SIDM. We find that clusters with only one bright CG show a median offset ~ 0.09 Mpc ($\sim 1'$) between the centroids of the 2D mass distribution and the BCG. However, this offset may be limited by the catalog-binning size, and some of those clusters may still be perturbed. Also, shape noise may contribute to this offset (McCleary et al. 2020).

To test those effects, we first reduce the binning size to 20×20 pixels and rebuild the mass maps in higher resolution. Since the smaller binning leads to much longer computational time, we only produce maps in the central $\sim 5\%-10\%$ region near the original peak and ensure the new central peak is within the window. This reanalysis indicates that the bin size reduction does not significantly change the trend between the

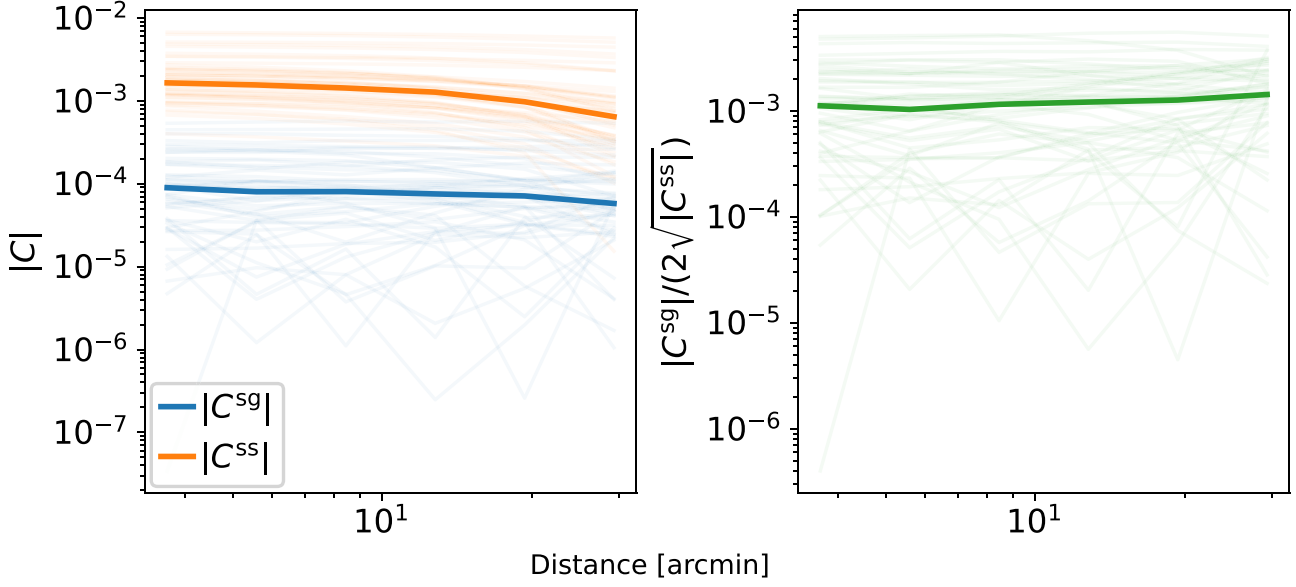


Figure 10. Left: star-galaxy shape correlations (C^{sg}) and star-star correlations (C^{ss}) in absolute values. Right: the effect of PSF modeling bias on the shear measurement. In both diagrams, the values in individual cluster fields are shown with low opacity, and their median values in each distance bin are shown in bold solid lines.

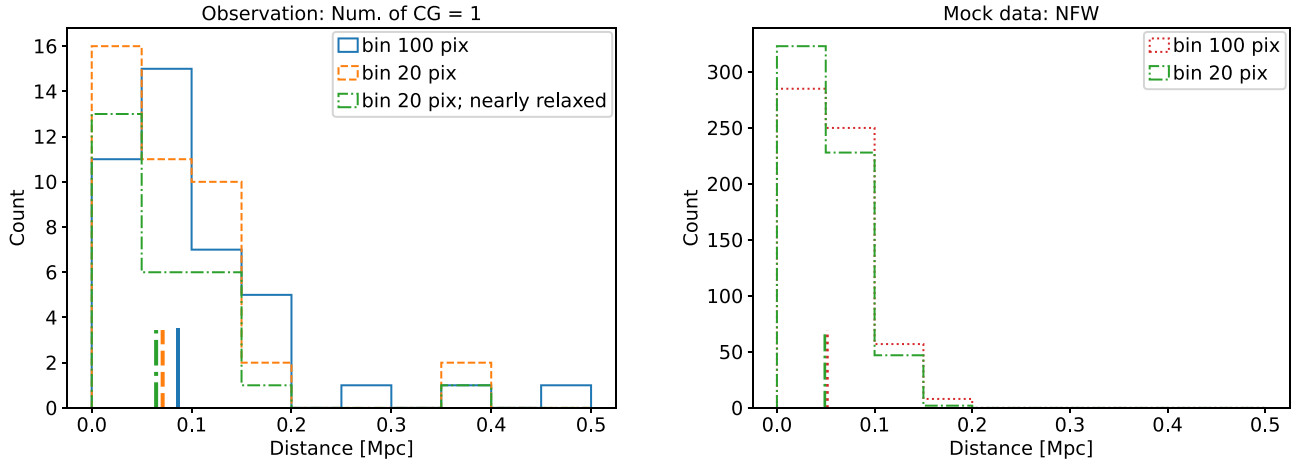


Figure 11. Left: histogram of mass-BCG center distance from observation. The blue solid curve corresponds to the distribution in Figure 9. The orange dashed curve shows the distribution of the same clusters under the 20 pixel binning. The green dashed-dotted curve shows the distribution of selected clusters with the 20 pixel binning. The vertical lines at the bottom give the median of each distribution. Right: histogram of the distance between the NFW halo center and the detected lensing peak derived from the mock data (600 runs).

aperture radius and the peak S/N. Additionally, we remove the clusters that have reported mergers (Section 4.1) or have clear signs of interaction at the BCG (e.g., a dumbbell shape with double cores) by visual inspection. Then, we remake the offset histogram and compare that with the previous result—the left panel of Figure 11 shows that the offset drops (median ~ 64 kpc) when we use smaller bins and more relaxed clusters.

Next, we study the contribution from shape noise by building mock shape catalogs distorted by a typical cluster in our sample with representative lensing sources. We consider a spherical NFW halo at redshift $z = 0.08$ with mass $M_{200c} = 7 \times 10^{14} M_{\odot}$, and we set the source galaxies at redshift $z = 0.7$ with per-component shape dispersion 0.4 and number density 7 arcmin^{-2} ; those are approximately the median values in our final catalogs for lensing analysis. Then, we bin the catalog by 100 pixels and 20 pixels, make mass maps, respectively, and measure the distance between the mass map central peak and the NFW halo center. The distributions of

their offsets derived from mock catalogs are shown in the right panel of Figure 11. For the 100 pixel binning, the median values in the real (nearly relaxed) and mock observations are ~ 90 kpc and ~ 52 kpc, respectively. Taking the square root of the difference between their squares (the intrinsic offset and the shape noise are independent), we conclude that the intrinsic/net offset is $\lesssim 73$ kpc. Similarly, under the 20 pixel binning, the median values in the real and mock observations are ~ 64 kpc and ~ 49 kpc, respectively, and we estimate a net offset $\lesssim 41$ kpc. Note that the true value could still be smaller since some clusters might not be fully relaxed, the sample size is limited, and there could be other contributing noise factors. Nonetheless, our result sets an upper limit of the intrinsic offset, which is still larger than the common values in SIDM tests ($\lesssim 10$ kpc) (e.g., Harvey et al. 2019). In the future, we will revisit this problem through the entire LoVoCCS sample, utilize the gas centroid (obtained from high-resolution X-ray observations) as a tracer of the mass peak, and use more

complete spectroscopic data to determine the dynamical state. We will further test the effect of shape noise using mock catalogs derived from cosmological simulations (e.g., Dietrich et al. 2012a). Another interesting follow-up study might examine the relationship between the offset and the BCG orientation.

6. Summary

In this work, we analyzed the complete DECam observations of 58 LoVoCCS clusters spanning a wide range of dynamical states, redshifts, and X-ray luminosities and produced their lensing mass and RS galaxy maps. The depth of observation is unprecedented for the majority of our clusters, and for about half of the sample, the WL maps presented in this work are the first in the literature.

We present and inspect the mass and galaxy distributions, and compare them with previous studies (Section 4.1). We also study the correlations between their orientation angles and centroids (Sections 4.2 and 4.3). Many clusters in our sample exhibit alignment between the orientations and/or centroids of the BCG and mass/galaxy distributions, without strong dependence on the dynamical state, redshift, and mass. The orientation alignment is stronger near the cluster center than the outer region, and it is stronger between the BCG and the RS galaxy distribution. The BCG and the RS distribution have a median misalignment angle of 19° within a radial cut of 2 Mpc; the median center offset is 0.09 Mpc. The mass and RS distributions show a median misalignment angle of 32° within 1 Mpc; the median center offset is 0.13 Mpc. Between the mass distribution and the BCG, the median misalignment angle within 0.5 Mpc is 35° , and the median center offset is 0.09 Mpc. Our results are comparable to recent studies of different samples (e.g., Umetsu et al. 2018). Additionally, Zhou et al. (2023) showed that the CG and member galaxy distribution are more closely aligned at lower redshift and higher cluster mass (i.e., the cluster evolution enhances the alignment), which is consistent with our results—our sample focuses on nearby massive clusters and show signs of stronger alignment between the CG and galaxy distribution compared to the literature.

We are actively acquiring additional spectroscopic redshifts of both background source galaxies and cluster members. Combined with anticipated contributions from the Dark Energy Spectroscopic Instrument (DESI) survey, future observations are expected to significantly enhance the spec-z completeness for LoVoCCS clusters, which will be instrumental in refining the calibration of photometric redshifts. Improved spec-z measurements will also enable more accurate determination of cluster galaxy membership and dynamical state, sharpening our detection of RS and blue cloud galaxies and providing valuable insights into the star formation histories of our cluster sample. In parallel, alternative methods for distinguishing red and blue cluster member galaxies are under study, such as the Gaussian mixture model-based Red Dragon algorithm (Black & Evrard 2022). The future scope of our work includes broadening the alignment studies to test the IA of cluster member galaxies, and to incorporate gas morphology via X-ray and SZ observations. We intend to utilize the distributions of mass, galaxies, and gas to explore splashback features in greater detail. Finally, the results of parametric mass fitting for LoVoCCS clusters will be detailed in an upcoming publication. Our data products, including coadded images and final

catalogs, will be made available to the research community, and interested parties can obtain the mass and galaxy maps from the corresponding author. The LoVoCCS DECam exposures are publicly available on the NOIRLab Astro Data Archive website.³⁷

Acknowledgments

We thank the anonymous reviewer for constructive comments that have helped improve the paper. We thank the LSST Data Management team and the CTIO observation support team. We thank Xiangchong Li, Chun-Hao To, Yuanyuan Zhang, Thomas Matheson, and Camille Avestruz for their comments and support. We thank the members of the Observational Cosmology, Gravitational Lensing and Astrophysics Research Group at Brown University for contributing to the tests of the LoVoCCS `run_steps` pipeline on different galaxy clusters, especially previous/current students and group members: Isabel Horst, Taylor Knapp, Derek Waleffe, Andrea Minot, Claire Hawkins, Alexandra Ekstrom, Natalie Rugg, Nicholas Conroy, Miguel Ruiz Granda, Liam Storan, Jessica Washington, Pei-Jun Huang, Francesco Serraino, Richard Dong, Youngik Lee, Dani Romero Mejia, Tim Launders, Vini Amit Rupchandani, and Alexander Green.

I.D. and D.C. are thankful for the support from the National Science Foundation (No. AST-2108287; Collaborative Research; LoVoCCS). G.W. gratefully acknowledges support from the National Science Foundation through grant AST-2205189 and from HST program No. GO-16300. M.D., D.T., and A.E. are grateful for support from the National Aeronautics and Space Administration Astrophysics Data Analysis Program (NASA-80NSSC22K0476). K.U. acknowledges support from the National Science and Technology Council of Taiwan (grant NSTC 112-2112-M-001-027-MY3) and from the Academia Sinica Investigator Award (AS-IA-112-M04). J.S. was supported by the National Research Foundation of Korea (NRF) grant funded by the Korean government (MSIT) (No. RS-2023-00210597). P.N. acknowledges support from DOE grant #DE-SC0017660. E.P. is supported by NASA grant 80NSSC23K0747. The work of S.F. and T.L. is supported by NOIRLab, which is managed by the Association of Universities for Research in Astronomy (AURA) under a cooperative agreement with the National Science Foundation.

This research was conducted using computational resources and services at the Center for Computation and Visualization, Brown University.

This work has made use of data from the European Space Agency (ESA) mission Gaia (<https://www.cosmos.esa.int/gaia>), processed by the Gaia Data Processing and Analysis Consortium (DPAC; <https://www.cosmos.esa.int/web/gaia/dpac/consortium>). Funding for the DPAC has been provided by national institutions, in particular, the institutions participating in the Gaia Multilateral Agreement.

The Pan-STARRS1 Surveys (PS1) and the PS1 public science archive have been made possible through contributions by the Institute for Astronomy, the University of Hawaii, the Pan-STARRS Project Office, the Max Planck Society and its participating institutes, the Max Planck Institute for Astronomy, Heidelberg and the Max Planck Institute for Extraterrestrial Physics, Garching, The Johns Hopkins University, Durham University, the University of Edinburgh, the Queen’s

³⁷ <https://astroarchive.noirlab.edu>

University Belfast, the Harvard-Smithsonian Center for Astrophysics, the Las Cumbres Observatory Global Telescope Network Incorporated, the National Central University of Taiwan, the Space Telescope Science Institute, the National Aeronautics and Space Administration under grant No. NNX08AR22G issued through the Planetary Science Division of the NASA Science Mission Directorate, the National Science Foundation grant No. AST-1238877, the University of Maryland, Eotvos Lorand University (ELTE), the Los Alamos National Laboratory, and the Gordon and Betty Moore Foundation. All the PS1 data used in this paper can be found in MAST doi:[10.17909/55E7-5X63](https://doi.org/10.17909/55E7-5X63) (STScI 2022).

The national facility capability for SkyMapper has been funded through ARC LIEF grant LE130100104 from the Australian Research Council, awarded to the University of Sydney, the Australian National University, Swinburne University of Technology, the University of Queensland, the University of Western Australia, the University of Melbourne, Curtin University of Technology, Monash University and the Australian Astronomical Observatory. SkyMapper is owned and operated by The Australian National University's Research School of Astronomy and Astrophysics. The survey data were processed and provided by the SkyMapper Team at ANU. The SkyMapper node of the All-Sky Virtual Observatory (ASVO) is hosted at the National Computational Infrastructure (NCI). Development and support of the SkyMapper node of the ASVO has been funded in part by Astronomy Australia Limited (AAL) and the Australian Government through the Commonwealth's Education Investment Fund (EIF) and National Collaborative Research Infrastructure Strategy (NCRIS), particularly the National eResearch Collaboration Tools and Resources (NeCTAR) and the Australian National Data Service Projects (ANDS).

Funding for SDSS has been provided by the Alfred P. Sloan Foundation, the Participating Institutions, the National Aeronautics and Space Administration, the National Science Foundation, the US Department of Energy, the Japanese Monbukagakusho, and the Max Planck Society. The SDSS website is <https://www.sdss.org>. SDSS is managed by the Astrophysical Research Consortium (ARC) for the Participating Institutions. The Participating Institutions are The University of Chicago, Fermilab, the Institute for Advanced Study, the Japan Participation Group, The Johns Hopkins University, Los Alamos National Laboratory, the Max-Planck-Institute for Astronomy (MPIA), the Max-Planck-Institute for Astrophysics (MPA), New Mexico State University, University of Pittsburgh, Princeton University, the United States Naval Observatory, and the University of Washington.

The VHS data products served at Astro Data Lab are based on observations collected at the European Organization for Astronomical Research in the Southern Hemisphere under ESO program 179.A-2010, and/or data products created thereof. Based on data obtained from the ESO Science Archive Facility with DOI:<https://doi.org/10.18727/archive/57>. Based on data products created from observations collected at the European Organization for Astronomical Research in the Southern Hemisphere under ESO program 179.A-2010 and made use of data from the VHS (McMahon et al. 2013) with data pipeline processing with the VISTA Data Flow System (Irwin et al. 2004; Lewis et al. 2010; Cross et al. 2012).

The HSC Collaboration includes the astronomical communities of Japan and Taiwan, and Princeton University. The HSC

instrumentation and software were developed by the National Astronomical Observatory of Japan (NAOJ), the Kavli Institute for the Physics and Mathematics of the Universe (Kavli IPMU), the University of Tokyo, the High Energy Accelerator Research Organization (KEK), the Academia Sinica Institute for Astronomy and Astrophysics in Taiwan (ASIAA), and Princeton University. Funding was contributed by the FIRST program from the Japanese Cabinet Office, the Ministry of Education, Culture, Sports, Science and Technology (MEXT), the Japan Society for the Promotion of Science (JSPS), Japan Science and Technology Agency (JST), the Toray Science Foundation, NAOJ, Kavli IPMU, KEK, ASIAA, and Princeton University. This paper makes use of software developed for the Large Synoptic Survey Telescope. We thank the LSST Project for making their code available as free software at <https://www.lsst.org/about/dm>. This paper is based [in part] on data collected at the Subaru Telescope and retrieved from the HSC data archive system, which is operated by the Subaru Telescope and Astronomy Data Center (ADC) at the National Astronomical Observatory of Japan. Data analysis was in part carried out with the cooperation of the Center for Computational Astrophysics (CfCA), National Astronomical Observatory of Japan. The Subaru Telescope is honored and grateful for the opportunity to observe the Universe from Maunakea, which has cultural, historical, and natural significance in Hawaii.

This research has made use of the Spanish Virtual Observatory (<https://svo.cab.inta-csic.es>) project funded by MCIN/AEI/10.13039/501100011033/ through grant PID2020-112949GB-I00.

This research has made use of NED, which is funded by the National Aeronautics and Space Administration and operated by the California Institute of Technology.

This research has made use of the SIMBAD database, operated at CDS, Strasbourg, France.

This research has made use of data, software, and/or web tools obtained from the High Energy Astrophysics Science Archive Research Center (HEASARC), a service of the Astrophysics Science Division at NASA/GSFC and of the Smithsonian Astrophysical Observatory's High Energy Astrophysics Division.

This project used data obtained with the Dark Energy Camera (DECam), which was constructed by the DES Collaboration. This work is based on observations at CTIO, NSF's NOIRLab (NOIRLab Prop. ID 2019A-0308; PI: I. Dell'Antonio). This project used public archival data from DES. Funding for the DES Projects has been provided by the US Department of Energy, the US National Science Foundation, the Ministry of Science and Education of Spain, the Science and Technology Facilities Council of the United Kingdom, the Higher Education Funding Council for England, the National Center for Supercomputing Applications at the University of Illinois at Urbana-Champaign, the Kavli Institute of Cosmological Physics at the University of Chicago, the Center for Cosmology and Astro-Particle Physics at the Ohio State University, the Mitchell Institute for Fundamental Physics and Astronomy at Texas A&M University, Financiadora de Estudos e Projetos, Fundação Carlos Chagas Filho de Amparo à Pesquisa do Estado do Rio de Janeiro, Conselho Nacional de Desenvolvimento Científico e Tecnológico and the Ministério da Ciência, Tecnologia e Inovação, the Deutsche Forschungsgemeinschaft, and the Collaborating Institutions in the DES. The Collaborating Institutions are Argonne National

Laboratory, the University of California at Santa Cruz, the University of Cambridge, Centro de Investigaciones Energéticas, Medioambientales y Tecnológicas-Madrid, the University of Chicago, University College London, the DES-Brazil Consortium, the University of Edinburgh, the Eidgenössische Technische Hochschule (ETH) Zürich, Fermi National Accelerator Laboratory, the University of Illinois at Urbana-Champaign, the Institut de Ciències de l'Espai (IEEC/CSIC), the Institut de Física d'Altes Energies, Lawrence Berkeley National Laboratory, the Ludwig-Maximilians Universität München and the associated Excellence Cluster Universe, the University of Michigan, the National Optical Astronomy Observatory, the University of Nottingham, The Ohio State University, the OzDES Membership Consortium, the University of Pennsylvania, the University of Portsmouth, SLAC National Accelerator Laboratory, Stanford University, the University of Sussex, and Texas A&M University. Based on observations at CTIO, a program of NOIRLab (NOIRLab Prop. 2012B-0001; PI J. Frieman).

The Legacy Surveys consist of three individual and complementary projects: the Dark Energy Camera Legacy Survey (DECaLS; Proposal ID #2014B-0404; PIs: David Schlegel and Arjun Dey), the Beijing-Arizona Sky Survey (BASS; NOAO Prop. ID #2015A-0801; PIs: Zhou Xu and Xiaohui Fan), and the Mayall z -band Legacy Survey (MzLS; Prop. ID #2016A-0453; PI: Arjun Dey). DECaLS, BASS, and MzLS together include data obtained, respectively, at the Blanco telescope, CTIO, NSF's NOIRLab; the Bok telescope, Steward Observatory, University of Arizona; and the Mayall telescope, Kitt Peak National Observatory, NOIRLab. The Legacy Surveys project is honored to be permitted to conduct astronomical research on Iolkam Du'ag (Kitt Peak), a mountain with particular significance to the Tohono O'odham Nation. BASS is a key project of the Telescope Access Programme (TAP), which has been funded by the National Astronomical Observatories of China, the Chinese Academy of Sciences (the Strategic Priority Research Programme "The Emergence of Cosmological Structures" grant No. XDB09000000), and the Special Fund for Astronomy from the Ministry of Finance. The BASS is also supported by the External Cooperation Programme of Chinese Academy of Sciences (grant No. 114A11KYSB20160057), and Chinese National Natural

Science Foundation (grant No. 11433005). The Legacy Survey team makes use of data products from the Near-Earth Object Wide-field Infrared Survey Explorer (NEOWISE), which is a project of the Jet Propulsion Laboratory/California Institute of Technology. NEOWISE is funded by the National Aeronautics and Space Administration. The Legacy Surveys imaging of the DESI footprint is supported by the Director, Office of Science, Office of High Energy Physics of the US Department of Energy under contract No. DE-AC02-05CH1123, by the National Energy Research Scientific Computing Center, a DOE Office of Science User Facility under the same contract; and by the US National Science Foundation, Division of Astronomical Sciences under contract No. AST-0950945 to NOAO.

This research uses services or data provided by the Astro Data Lab at NSF's NOIRLab.

This research is based on data obtained from the Astro Data Archive at NSF's NOIRLab. These data are associated with the observing programs listed in Table 3.

Facility: Blanco, Astro Data Lab, Astro Data Archive, IRSAC
Software: Astropy (Astropy Collaboration et al. 2013, 2018, 2022), Astroquery (Ginsburg et al. 2019), LSST Science Pipelines (Jurić et al. 2017; Bosch et al. 2019), Matplotlib (Hunter 2007), NumPy (Harris et al. 2020), SciPy (Virtanen et al. 2020), Source Extractor (Bertin & Arnouts 1996).

Appendix A Survey Depth

We use Tables 1 and 2 to show the 5σ depth of the cluster fields ($\sim 2^\circ$ in diameter) whose maps are presented in Section 4.1. Those LoVoCCS clusters are observation-time complete. We consider an annular region from a radial distance of $10'$ to 1° toward the cluster in each field to reduce the contamination effect of cluster member galaxies, although some fields include scattered cluster pairs/groups (e.g., A401/A399, A3827/A3825, and A2556/A2554); as the background galaxies are much fainter and greatly outnumber the foreground galaxies, we expect the statistical bias caused by member galaxies is minimal.

Table 1
Cluster Field Depth (Part I)

Name	R.A. (deg)	Decl. (deg)	u_{p5}	g_{p5}	r_{p5}	i_{p5}	z_{p5}	u_{c5}	g_{c5}	r_{c5}	i_{c5}	z_{c5}
A2029	227.73	5.82	24.9	26.7	26.3	25.5	25.0	24.6	26.4	25.9	25.1	24.6
A401	44.74	13.58	24.7	25.5	25.7	25.1	24.2	24.4	25.2	25.3	24.8	23.9
A85	10.40	-9.33	25.3	25.8	26.0	25.1	23.4	25.0	25.5	25.7	24.8	23.1
A3667	303.14	-56.84	25.3	26.2	26.3	25.8	25.2	25.1	25.8	25.9	25.2	24.7
A3266	67.80	-61.41	25.3	26.3	26.1	25.6	24.8	25.0	26.0	25.8	25.2	24.5
A1651	194.84	-4.20	25.2	25.5	26.0	25.5	24.5	24.9	25.3	25.7	25.1	24.2
A754	137.21	-9.64	25.7	26.1	25.9	25.3	25.2	25.5	25.8	25.5	25.0	24.8
A3571	206.87	-32.87	25.3	25.9	26.1	25.3	24.6	25.0	25.7	25.8	25.1	24.4
A3112	49.47	-44.24	25.4	25.5	26.3	25.4	24.4	25.1	25.3	26.0	25.1	24.1
A2597	351.33	-12.12	25.2	26.1	26.1	25.4	25.0	25.0	25.9	25.8	25.1	24.7
A1650	194.68	-1.76	25.2	26.0	25.7	25.9	25.0	24.9	25.7	25.4	25.6	24.6
A3558	201.98	-31.49	25.3	26.3	26.0	25.3	24.6	25.0	26.0	25.7	24.9	24.3
A3695	308.70	-35.83	25.2	26.1	26.1	25.9	25.0	24.9	25.9	25.8	25.5	24.7
A3921	342.50	-64.43	25.2	25.6	26.0	25.5	24.3	25.0	25.4	25.7	25.2	24.0
A2426	333.61	-10.37	25.4	26.0	26.1	25.6	24.5	25.2	25.7	25.8	25.3	24.2
A3158	55.66	-53.63	25.4	25.6	26.2	25.2	24.4	25.1	25.3	25.4	24.9	24.1

Table 1
(Continued)

Name	R.A. (deg)	Decl. (deg)	u_{p5}	g_{p5}	r_{p5}	i_{p5}	z_{p5}	u_{c5}	g_{c5}	r_{c5}	i_{c5}	z_{c5}
RXCJ1217.6+0339	184.43	3.65	25.0	24.8	25.8	26.1	23.6	24.8	24.5	25.4	25.8	23.3
A2811	10.54	-28.54	25.6	26.2	26.1	25.5	24.9	25.3	25.9	25.8	25.1	24.6
A780	139.62	-12.26	25.5	26.0	26.0	25.3	24.4	25.2	25.8	25.7	25.0	24.0
A2420	332.59	-12.19	25.3	25.9	26.1	25.4	24.8	25.1	25.7	25.8	25.1	24.5
A1285	172.61	-14.56	25.0	25.7	26.0	25.1	24.4	24.8	25.5	25.6	24.8	24.1
A3911	341.59	-52.74	25.5	25.9	26.2	25.6	24.3	25.3	25.7	25.8	25.3	24.0
A2055	229.69	6.23	25.1	25.5	25.9	25.4	24.6	24.8	25.2	25.6	25.1	24.3
A1750	202.71	-1.86	25.0	26.0	26.0	25.4	24.7	24.7	25.8	25.6	25.1	24.4
A3822	328.53	-57.85	25.2	26.2	25.9	25.5	24.6	24.9	26.0	25.6	25.2	24.3
A2941	26.27	-53.02	25.4	25.9	26.0	25.1	24.5	25.1	25.7	25.7	24.8	24.1
A2440	335.97	-1.60	24.9	25.6	25.9	25.2	24.5	24.6	25.4	25.6	24.9	24.1
A1644	194.30	-17.41	25.1	26.2	26.1	25.3	24.6	24.8	25.9	25.8	25.1	24.3

Note. We show the 5σ PSF magnitudes of point sources (m_{p5}) and CModel magnitudes of extended sources (m_{c5}) in the DECam u , g , r , i , z bands of individual cluster fields (sorted by X-ray luminosity/cluster rank) and their median values (Table 2). These are apparent AB magnitudes without Galactic extinction correction ($\lesssim 0.1$ mag in the r band). The magnitude zero-points have been corrected for the color terms between the reference catalogs (PS1/SkyMapper/SDSS) and DECam, and here we only consider the magnitude uncertainties reported in the LSST pipeline forced photometry of coadded images. The residual zero-point offsets are $\lesssim 0.03$ mag in g , r , i , z when compared with DES (if available) and $\lesssim 0.05$ mag in u when compared with model stellar loci in the color–color space. The celestial coordinates come from SIMBAD (ICRS, J2000).

Table 2
Cluster Field Depth (Part II)

Name	R.A. (deg)	Decl. (deg)	u_{p5}	g_{p5}	r_{p5}	i_{p5}	z_{p5}	u_{c5}	g_{c5}	r_{c5}	i_{c5}	z_{c5}
A1348	175.35	-12.27	25.4	26.1	25.9	26.2	24.7	25.1	25.9	25.6	25.9	24.4
RBS1847	334.50	-65.18	25.2	26.1	26.0	25.0	24.1	24.9	25.8	25.7	24.7	23.8
RXCJ1215.4-3900	183.89	-38.99	25.4	25.7	25.6	25.0	24.6	25.0	25.4	25.3	24.7	24.2
A2351	323.60	-13.39	25.3	25.8	26.1	25.2	24.3	25.0	25.6	25.8	24.9	24.0
RXCJ2218.2-0350	334.58	-3.83	25.2	25.7	25.8	24.9	24.1	24.9	25.5	25.5	24.6	23.7
A2443	336.56	17.42	25.0	26.0	26.0	25.0	24.5	24.7	25.6	25.6	24.7	24.1
A2050	229.08	0.06	25.3	26.3	26.2	25.7	24.8	25.0	26.0	25.9	25.3	24.5
A1736	201.72	-27.11	24.8	26.7	26.5	25.4	24.5	24.5	26.4	26.0	25.0	24.2
A2384	328.08	-19.61	25.5	25.6	25.9	25.2	25.0	25.2	25.3	25.6	24.9	24.6
A4059	359.17	-34.67	25.4	25.8	25.9	25.3	24.3	25.1	25.5	25.6	25.0	24.1
A3836	332.40	-51.84	25.0	26.6	25.9	25.5	24.1	24.7	26.3	25.6	25.2	23.8
A2533	346.81	-15.22	25.2	26.0	25.5	25.0	24.3	25.0	25.7	25.2	24.8	24.0
A2556	348.26	-21.63	25.3	25.8	25.7	25.3	24.7	25.0	25.5	25.4	25.0	24.3
A3126	52.18	-55.71	24.8	25.9	26.1	25.0	24.2	24.5	25.7	25.8	24.8	23.9
RXCJ0049.4-2931	12.35	-29.53	25.1	25.7	26.0	25.3	24.6	24.9	25.5	25.7	25.0	24.3
A3395	96.88	-54.40	25.4	26.2	26.3	25.7	25.1	25.0	25.9	25.9	25.2	24.6
A1606	191.15	-11.99	24.4	26.1	26.1	25.8	24.6	24.1	25.8	25.7	25.5	24.4
A2670	358.54	-10.39	24.9	24.8	25.9	25.3	24.6	24.7	24.6	25.5	25.0	24.4
A3532	194.33	-30.37	25.4	26.3	25.9	25.0	24.3	25.1	26.0	25.6	24.8	24.0
RXCJ1139.4-3327	174.86	-33.45	25.5	26.1	26.0	25.5	24.1	25.1	25.8	25.7	25.0	23.8
RXJ0820.9+0751	125.26	7.86	25.0	25.8	26.1	25.7	24.9	24.7	25.5	25.8	25.3	24.5
A3128	52.64	-52.55	25.9	26.4	26.3	25.4	24.9	25.6	26.1	25.6	25.1	24.5
A1023	157.00	-6.80	25.2	26.1	26.0	25.1	24.2	24.9	25.7	25.7	24.7	23.8
A3528	193.58	-29.02	24.9	25.8	26.3	25.3	24.6	24.6	25.6	26.0	25.1	24.3
A761	137.65	-10.58	25.5	26.2	26.0	25.3	24.6	25.2	25.9	25.7	25.0	24.3
A3825	329.59	-60.39	25.3	26.1	26.1	25.8	24.0	25.0	25.8	25.3	25.3	23.7
Median	25.3	26.0	26.0	25.3	24.6	25.0	25.7	25.7	25.1	24.2

Appendix B DECam Archival Data

In Table 3, we list the proposal IDs of the public exposures used in our coaddition. We thank the researchers of those programs for their observations.

Table 3
DECam Public Data Sets Used in Our Coaddition (Sorted by Proposal ID)

PROPID	PI	PROPID	PI	PROPID	PI	PROPID	PI
2012B-0001	Frieman	2014A-0270	Grillmair	2016A-0189	Rest	2018A-0911	Forster
2012B-0003	DES SV	2014A-0306	Dai	2016A-0190	Dey	2018A-0913	Zenteno
2012B-0569	Allen	2014A-0321	Geha	2016A-0366	Bechtol	2018A-0914	Makler
2012B-3004	Dell' Antonio	2014A-0339	Hargas	2016A-0384	McCleary	2018B-0905	Oh
2012B-3007	Thorman	2014A-0386	Dell' Antonio	2016A-0386	Malhotra	2019A-0205	Goldstein
2012B-9999	Engineering	2014A-0390	Bloom	2016A-0397	Zenteno	2019A-0265	Finkbeiner
2013A-0327	Rest	2014A-0412	Rest	2016A-0618	Mackey	2019A-0272	Zenteno
2013A-0360	von der Linden	2014A-0415	von der Linden	2016A-0622	Penny	2019A-0305	Drlica-Wagner
2013A-0400	Bloom	2014A-0608	Forster	2016A-0951	Bechtol	2019A-0308	Dell' Antonio
2013A-0411	Nidever	2014A-0610	Taylor	2016B-0124	Frieman	2019A-0913	Carballo-Bello
2013A-0455	Sheppard	2014A-0613	Rodriguez	2016B-0301	Rest	2019A-0917	Lopes
2013A-0529	Rich	2014A-0621	Mackey	2016B-0905	Jerjen	2019B-0323	Zenteno
2013A-0611	Mackey	2014A-0624	Jerjen	2016B-0909	Navarete	2019B-0372	Soares-Santos
2013A-0612	Sheen	2014B-0146	Sullivan	2017A-0260	Soares-Santos	2019B-0403	Martinez-Vazquez
2013A-0613	Munoz	2014B-0244	von der Linden	2017A-0388	Zenteno	2019B-1004	Chaname
2013A-0704	Wood	2014B-0265	Dell' Antonio	2017A-0909	Cooke	2019B-1014	Olivares
2013A-0717	Dell' Antonio	2014B-0404	Schlegel	2017A-0916	Carballo-Bello	2020A-0399	Zenteno
2013A-0719	Saha	2014B-0608	Jaffe	2017A-0925	Munoz	2020A-0402	Vivas
2013A-0724	Allen	2015A-0062	French	2017B-0103	Barkhouse	2020A-0908	Olivares
2013A-0737	Sheppard	2015A-0110	De Boer	2017B-0110	Frieman	2020A-0909	Arevalo
2013A-0741	Schlegel	2015A-0163	Grillmair	2017B-0253	Carlin	2020B-0053	Shen
2013A-2101	Walker	2015A-0306	Balbinot	2017B-0279	Rest	2020B-0241	Zenteno
2013A-9999	Lee	2015A-0397	Walker	2017B-0904	Lopes	2020B-0909	Chaname
2013B-0418	Rest	2015A-0608	Forster	2017B-0907	Munoz	2021A-0117	Kotulla
2013B-0421	Rest	2015A-0609	Carballo-Bello	2017B-0951	Vivas	2021A-0149	Zenteno
2013B-0440	Nidever	2015A-0616	Jerjen	2018A-0215	Carlin	2021A-0275	Rest
2013B-0502	Dell	2015A-0617	Nataf	2018A-0242	Bechtol	2021A-0922	Nilo-Castellon
2013B-0531	Rest	2015A-0618	Lidman	2018A-0276	Dell' Antonio	2022A-388025	Palmese & Wang
2013B-0612	Chaname	2015A-0619	Goncalves	2018A-0369	Rest	2022A-777564	Zhao
2013B-0617	Mackey	2015A-0620	Bonaca	2018A-0380	Rest	2022A-975778	Kelkar
2013B-0627	Lima Neto	2015B-0187	Berger	2018A-0386	Zenteno	2022B-297190	Palmese & Wang
2014A-0157	Favia	2015B-0191	Rice	2018A-0907	Munoz
2014A-0256	Eckert	2016A-0004	Bonaca	2018A-0909	Puzia

Appendix C Mass Map Example

We present an example of using the aperture mass map to detect the orientation (and center) of an elliptical NFW halo. We apply the Schirmer aperture to a mock lensing catalog derived from the study of Fu et al. (2024) (see also Oguri et al. 2010 and Oguri 2010). The catalog spans 24k \times 24k DECam pixels

(6×6 patches). The halo mass, source, and lens redshifts, shape noise, and source density are set to be the median values in our LoVoCCS observations (see also Section 5.3). In Figure 12, we show the convergence of the elliptical halo ($\kappa(\theta_1, \theta_2) = \kappa_{\text{NFW}}(\sqrt{q\theta_1^2 + \theta_2^2}/q)$; $q = 2/3$) overlaid with the lensing mass S/N map. The orientations of the halo and the map are generally consistent.

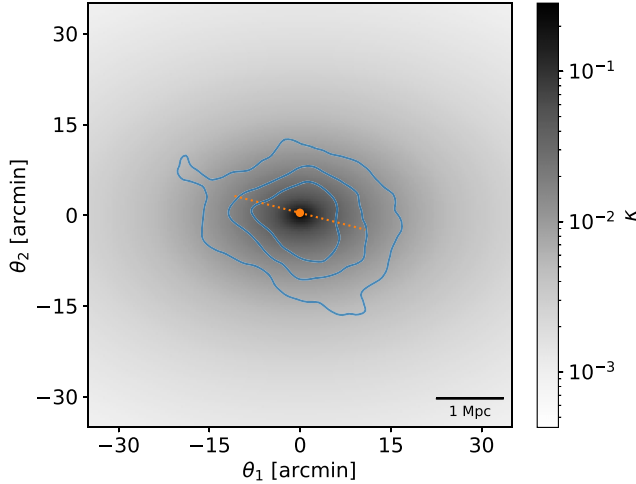


Figure 12. Convergence of an elliptical halo (centered in the diagram and elongated horizontally; gray scale in the background) overlaid with the corresponding aperture mass map (blue contours showing $S/N = 2, 4, 6$). The orange point and the dotted line give the detected lensing peak and the derived orientation angle (within 1 Mpc), respectively. We vary the aperture radius and use the aperture when the peak S/N reaches the maximum (10k pixels $\sim 10r_s$). The diagram spans 16k \times 16k DECam pixels (4×4 patches; $0.^{\prime\prime}263 \text{ pixel}^{-1}$), which is consistent with the figures in Section 4.1.

Appendix D RS Examples

We present examples of detecting and selecting the RS galaxies in the CMDs in Figure 13 (A3558) and Figure 14

(A3667). Those two clusters have enough spec-z data to show RS in CMD, and thus, we use the RS linear fit parameters detected from the spec-z selected galaxies instead of all galaxies (though their fitting results are close). The algorithm was presented in Section 3.4.

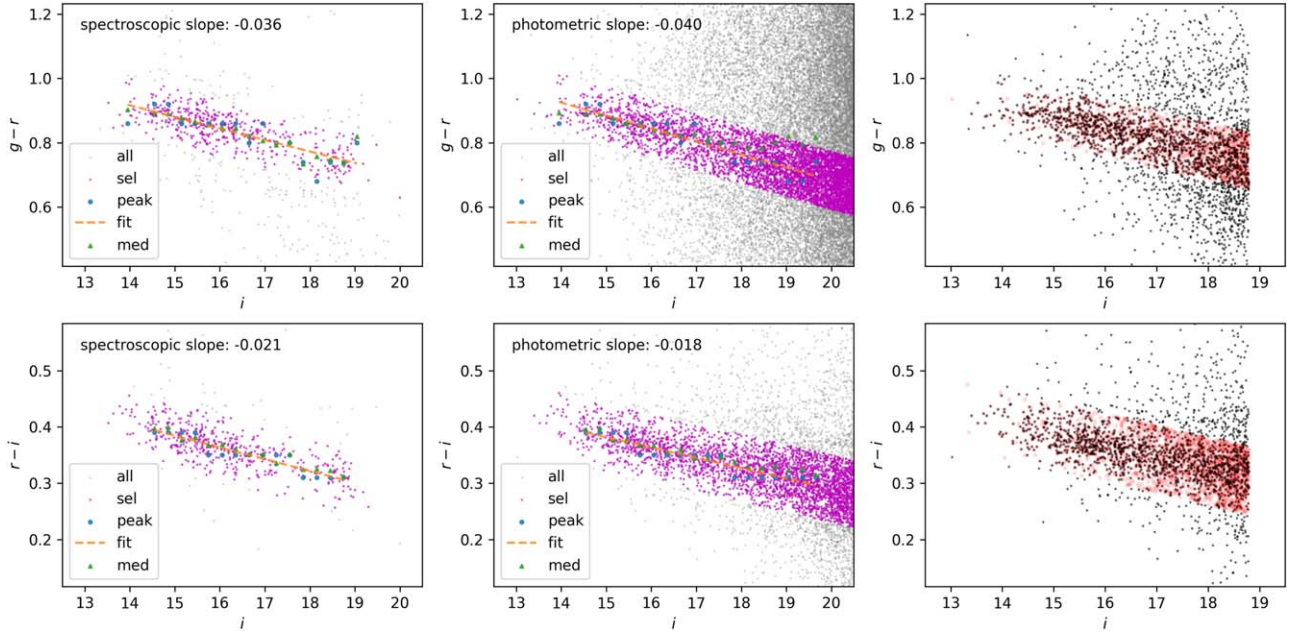


Figure 13. RS examples in A3558 ($z = 0.047$). Top left: the gray points are all member galaxies selected by spec-z. The blue points are the histogram peaks of those gray points in individual i -magnitude bins (Section 3.4), while the green triangles are the median values in those bins (consistent with blue points generally). The orange dashed line is the linear fit of those blue points. The magenta points are the galaxies selected by the scatter cut around the fitted line. Bottom left: the gray points are member galaxies selected by both spec-z and $g - r$ (i.e., the galaxies denoted by magenta points in the top left diagram)—the RS is clearer. Other markers have similar meanings to the ones in the top left diagram. Top middle: now the gray points are all galaxies in the catalog with valid photometry. Other markers have similar meanings to the top left diagram. Note the green median points have large biases at faint magnitudes, but the blue peak points are consistent with the trend at the bright end. Bottom middle: the gray points correspond to the magenta ones in the top middle diagram. Other markers have similar meanings. Again, the RS is more clear than its top counterpart because of the first selection in $g - r$. Top right: we start from all galaxies. The red circles show the galaxies selected by the $g - r$ fit (the spectroscopic one in this case), while the black points are the galaxies selected by the $r - i$ fit. Here, an extra i -magnitude cut is also included to fix the luminosity limit. The overlap between red and black points is the RS galaxy sample. Bottom right: similar to the top right diagram—the red-filled circles are selected by the $r - i$ fit, while the black-filled circles are selected by the $g - r$ fit. Those diagrams indicate that a single-color selection can include foreground/background galaxies, but a two-color selection can give a much cleaner sample of RS galaxies.

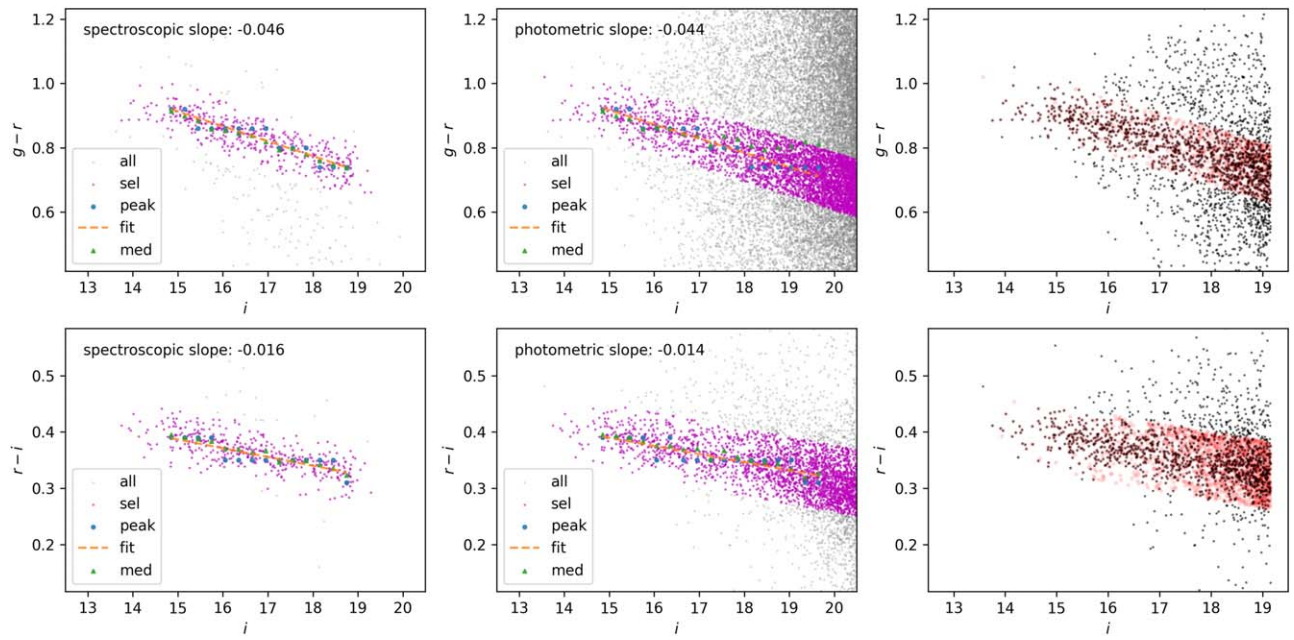


Figure 14. Counterparts of the RS examples in A3667 ($z = 0.055$). They are similar to the ones for A3558 (Figure 13).

Appendix E Orientations and Centers

Tables 4 and 5 show the measured orientation angles and centers of the BCG, the RS, and mass distributions (with different radial cuts) of individual clusters (and their types/CG counts).

We also examine the distributions of those angles (Figure 15). The distributions are generally uniform. Large radial cuts may lead to large noise in the angle measurement because at large radii the number density of member galaxies and the mass density are low.

Table 4
Cluster Centers and Orientation Angles (Part I)

Name	z	α_B	δ_B	α_M	δ_M	α_R	δ_R	θ_B	θ_{M5}	θ_{M10}	θ_{M20}	θ_{RS}	θ_{R10}	θ_{R20}	n_{CG}
A2029	0.08	227.73	5.74	227.73	5.78	227.74	5.77	-63	85	84	-70	-74	-74	-84	a
A401	0.07	44.74	13.58	44.74	13.58	44.74	13.58	-63	-7	1	-25	-61	-48	-58	a
A85	0.06	10.46	-9.30	10.45	-9.33	10.41	-9.31	59	-70	-84	-41	85	72	75	b
A3667	0.06	303.11	-56.83	303.14	-56.85	303.15	-56.84	44	-69	80	-84	38	44	48	a
A3827	0.10	330.47	-59.95	330.46	-59.94	330.48	-59.94	72	78	69	57	73	64	83	a
A3266	0.06	67.81	-61.45	67.80	-61.43	67.82	-61.45	-10	-74	80	86	-25	-24	-44	a
A1651	0.08	194.84	-4.20	194.83	-4.20	194.85	-4.20	-13	21	23	-66	-6	-2	-10	a
A754	0.05	137.13	-9.63	137.14	-9.65	137.12	-9.63	22	29	35	51	19	21	8	a
A3571	0.04	206.87	-32.86	206.89	-32.91	206.85	-32.88	-85	65	62	18	84	88	86	a
A3112	0.08	49.49	-44.24	49.49	-44.27	49.50	-44.22	-84	-75	-87	82	-53	-68	84	a
A399	0.07	44.47	13.03	44.46	13.03	44.44	13.02	-43	-33	-10	-10	-64	-34	-40	a
A2597	0.08	351.33	-12.12	351.32	-12.13	351.31	-12.11	50	68	-67	-66	52	81	76	a
A1650	0.08	194.67	-1.76	194.67	-1.78	194.68	-1.77	71	43	54	11	70	65	67	a
A3558	0.05	201.99	-31.50	201.98	-31.48	201.97	-31.52	74	70	67	54	47	45	11	a
A3695	0.09	308.69	-35.82	308.69	-35.83	308.69	-35.78	63	42	3	-12	54	80	82	a
A3921	0.09	342.49	-64.43	342.48	-64.35	342.44	-64.43	-5	-76	-39	-23	0	5	-11	a
A2426	0.10	333.63	-10.37	333.63	-10.35	333.64	-10.37	-5	77	82	68	-14	-11	76	a
A3158	0.06	55.72	-53.63	55.75	-53.65	55.75	-53.64	3	-77	-22	44	13	33	56	a
RXCJ1217.6+0339	0.08	184.42	3.66	184.40	3.64	184.43	3.67	-82	-29	-32	21	-22	-45	-56	a
A2811	0.11	10.54	-28.54	10.54	-28.54	10.54	-28.54	41	-7	50	53	6	35	31	a
A780	0.05	139.52	-12.10	139.52	-12.12	139.53	-12.12	59	3	33	49	68	68	59	a
A2420	0.08	332.58	-12.17	332.57	-12.16	332.56	-12.19	-42	16	13	-63	-64	-54	-44	a
A1285	0.11	172.60	-14.58	172.58	-14.59	172.59	-14.58	32	47	44	52	31	62	61	b
A3911	0.10	341.56	-52.72	341.54	-52.72	341.52	-52.69	46	-25	3	-4	40	55	55	a
A2055	0.10	229.69	6.23	229.73	6.26	229.69	6.25	65	57	-76	-62	58	66	68	c
A1750	0.09	202.71	-1.86	202.78	-1.73	202.71	-1.87	-11	-58	-59	20	-46	-56	-50	c
A3822	0.08	328.52	-57.87	328.55	-57.87	328.55	-57.85	-64	-23	63	39	-26	-46	-51	b

Table 4
(Continued)

Name	z	α_B	δ_B	α_M	δ_M	α_R	δ_R	θ_B	θ_{M5}	θ_{M10}	θ_{M20}	θ_{R5}	θ_{R10}	θ_{R20}	n_{CG}
A2941	0.12	26.24	-53.02	26.31	-53.06	26.28	-53.02	3	85	-78	33	14	23	30	b
A2440	0.09	335.99	-1.58	336.00	-1.60	335.97	-1.62	-34	3	25	19	-44	-41	-47	c

Note. We present the measurements of the BCG (B), the lensing mass distribution (M), and the RS galaxy distribution (R) of each LoVoCCS cluster studied in this work (sorted by X-ray luminosity/cluster rank). The redshift (z) is from SIMBAD. The coordinates (α/δ for R.A./decl. in ICRS) and angles (θ) are in degrees. The angles are counterclockwise from the X -axis, with the X -axis pointing to the west and the Y -axis pointing to the north. We present the angles within 0.5 Mpc, 1.0 Mpc, and 2.0 Mpc from the central peak with tags 5, 10, and 20, respectively. The last column (n_{CG}) gives the cluster type based on the number of bright central galaxies; 1, 2, ≥ 3 correspond to type a, b, c (43, 8, 7 clusters, respectively). We skip the noisy mass/RS distribution results of some clusters.

Table 5
Cluster Centers and Orientation Angles (Part II)

Name	z	α_B	δ_B	α_M	δ_M	α_R	δ_R	θ_B	θ_{M5}	θ_{M10}	θ_{M20}	θ_{R5}	θ_{R10}	θ_{R20}	n_{CG}
A1644	0.05	194.30	-17.41	194.30	-17.41	194.38	-17.25	-44	-80	83	52	75	89	76	a
A1348	0.12	175.35	-12.28	175.35	-12.27	175.38	-12.26	-10	-12	-20	82	-19	-14	-36	a
RBS1847	0.10	334.50	-65.18	334.46	-65.14	334.50	-65.17	-7	62	-84	-17	-46	-46	-69	a
RXCJ1215.4-3900	0.12	183.86	-39.03	183.87	-39.01	183.83	-39.05	-33	88	-70	-21	-41	-50	-73	a
A2351	0.09	323.57	-13.43	323.58	-13.42	323.57	-13.42	62	-69	-87	-82	56	71	74	a
RXCJ2218.2-0350	0.09	334.67	-3.78	334.56	-3.80	334.67	-3.77	2	-9	-42	46	-51	-32	-37	c
A2443	0.11	336.53	17.36	336.54	17.36	336.52	17.39	-55	87	85	80	74	63	61	c
A2050	0.12	229.07	0.09	229.08	0.08	229.07	0.08	-49	-80	67	48	-38	-34	-45	a
A1736	0.04	201.70	-27.14	201.71	-27.11	201.71	-27.13	77	-59	-38	-29	-77	85	-85	c
A2384	0.09	328.09	-19.55	328.09	-19.56	328.08	-19.55	-61	-56	-56	-26	85	-78	-82	b
A4059	0.05	359.25	-34.76	359.21	-34.79	359.25	-34.74	62	83	-72	25	53	54	74	a
A3836	0.11	332.34	-51.81	332.34	-51.80	332.35	-51.81	20	29	23	26	81	74	55	a
A2533	0.11	346.81	-15.22	346.86	-15.23	346.81	-15.21	-48	44	52	76	-49	-67	-72	a
A2556	0.09	348.26	-21.63	348.26	-21.65	42	10	8	24	a
A3126	0.08	52.15	-55.71	52.15	-55.71	52.15	-55.71	-66	85	87	-75	76	45	76	a
RXCJ0049.4-2931	0.11	12.35	-29.52	12.36	-29.52	12.34	-29.52	35	29	28	24	75	-83	67	a
A2554	0.11	348.08	-21.50	348.08	-21.49	348.07	-21.49	-85	-12	-5	2	-73	-72	47	a
A2033	0.08	227.86	6.35	-36	a
A3395	0.05	96.90	-54.45	96.67	-54.59	96.85	-54.45	34	45	82	-74	35	28	45	b
A1606	0.10	191.15	-11.99	191.15	-12.01	191.15	-12.01	-80	64	48	75	-68	56	26	a
A2670	0.08	358.56	-10.42	358.54	-10.41	358.56	-10.41	30	-62	19	54	85	-65	-63	a
A3532	0.06	194.34	-30.36	194.33	-30.36	194.32	-30.37	-8	-27	3	58	-40	-26	-13	a
RXCJ1139.4-3327	0.11	174.85	-33.45	174.83	-33.46	174.85	-33.44	77	-70	85	-38	-85	-84	78	a
RXJ0820.9+0751	0.11	125.26	7.86	125.26	7.87	125.27	7.86	15	-56	87	-74	8	45	-39	a
A3128	0.06	52.66	-52.62	52.64	-52.53	52.62	-52.56	-81	-80	78	50	-86	-87	-64	c
A1023	0.12	156.99	-6.80	157.00	-6.79	156.99	-6.79	49	27	-20	-32	44	53	75	a
A3528	0.06	193.59	-29.01	193.61	-29.00	193.59	-29.00	89	-86	-76	-87	-89	77	75	b
A761	0.09	137.65	-10.58	137.65	-10.59	137.68	-10.59	1	-56	32	-48	35	18	1	a
A3825	0.07	329.61	-60.39	329.62	-60.36	80	-78	-77	-7	b	

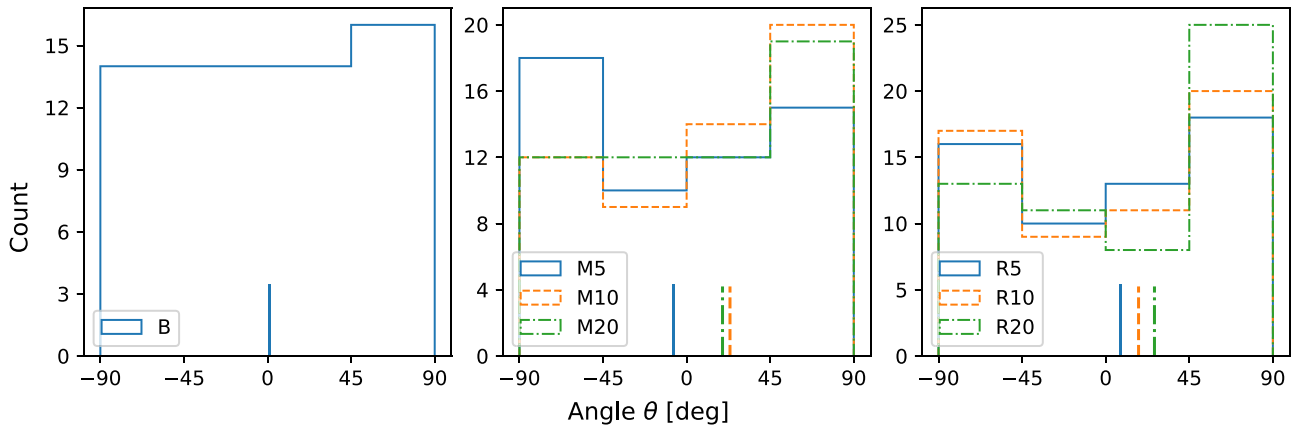


Figure 15. Angle distributions. The labels have the same meanings as the ones in Tables 4 and 5. The vertical lines give the respective median values.

Appendix F

Significance of Orientation Alignment

Consider a set of angles $\{\theta_i\}$, $i = 1, 2, \dots, N$. Each angle independently obeys a uniform distribution $\theta_i \sim U(0, \Phi)$. The probability of an angle θ_i being smaller than ϕ is ϕ/Φ . The probability of n angles being smaller than ϕ (and the others being larger than ϕ) is $\binom{N}{n}(\phi/\Phi)^n(1 - \phi/\Phi)^{N-n}$. Then the probability that more than m angles have their values smaller than ϕ is $\sum_{i=m+1}^N \binom{N}{i}(\phi/\Phi)^i(1 - \phi/\Phi)^{N-i} = 1 - F(m; N, \phi/\Phi)$, where F is the cumulative distribution function of a binomial distribution with m times of successes in N independent tests and success probability ϕ/Φ .

This result can be extended to the case where θ_i is between α and β . If $\alpha < \beta < \Phi$ and $\psi = \beta - \alpha$, the probability that more than m angles have values between α and β is similarly $1 - F(m; N, \psi/\Phi)$.

Let θ_i be the angle between two orientations (e.g., BCG and RS distribution) and Φ be the angle upper limit (90°). Let N be the number of clusters (e.g., 57 in our analysis after removing the noisy cluster). If we assume the angle is randomly distributed between 0° and 90° , then the probability that more than a fraction of f of those clusters have angles smaller than ϕ is $1 - F(57f; 57, \phi/90)$. Figure 16 gives this probability as a function of the fraction f and the angle cut ϕ . The probability drops quickly as the angle cut drops or the fraction increases. For example, the probability that more than one-third of the clusters have angles smaller than 30° is $1 - F(57/3; 57, 30/90) \sim 0.4$, the probability that more than half of the cluster sample has angles below 30° is $\sim 5 \times 10^{-3}$, and the probability that more than half of the sample has the angles below 15° is $\sim 3 \times 10^{-9}$.

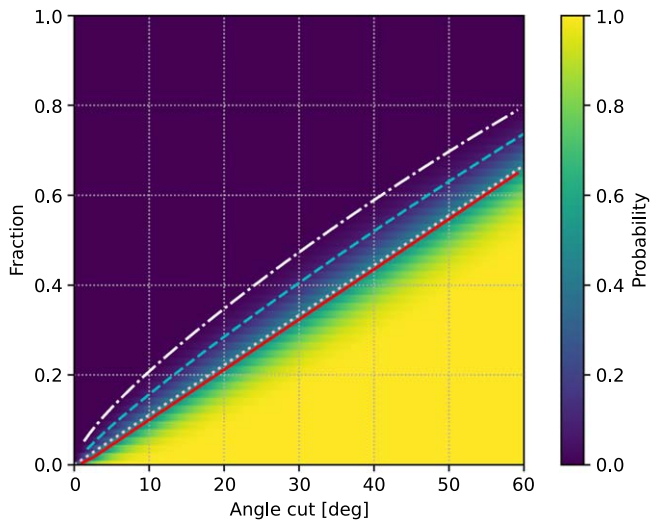


Figure 16. Probability of more than a fraction of the clusters having angles smaller than an angle cut. The red solid line, the cyan dashed line, and the white dashed-dotted line correspond to probabilities of 0.5, 0.1, and 0.01, respectively. The pink-dotted line gives the angle cut divided by 90° for reference.

ORCID iDs

Shenming Fu <https://orcid.org/0000-0001-5422-1958>
 Ian Dell'Antonio <https://orcid.org/0000-0003-0751-7312>
 Zacharias Escalante <https://orcid.org/0000-0003-0936-7223>
 Jessica Nelson <https://orcid.org/0000-0003-3397-6838>
 Anthony Englert <https://orcid.org/0000-0003-2314-5336>
 Søren Helhoski <https://orcid.org/0000-0003-4774-4288>
 Rahul Shinde <https://orcid.org/0000-0002-7342-3229>
 Christelyn Larkin <https://orcid.org/0009-0004-7248-8866>
 William K. Black <https://orcid.org/0000-0003-4811-7913>
 Ranga-Ram Chary <https://orcid.org/0000-0001-7583-0621>
 Douglas Clowe <https://orcid.org/0000-0003-2416-1557>
 M. C. Cooper <https://orcid.org/0000-0003-1371-6019>
 Megan Donahue <https://orcid.org/0000-0002-2808-0853>
 August Evrard <https://orcid.org/0000-0002-4876-956X>
 Mark Lacy <https://orcid.org/0000-0002-3032-1783>
 Tod Lauer <https://orcid.org/0000-0003-3234-7247>
 Binyang Liu <https://orcid.org/0000-0002-0561-7937>
 Jacqueline McCleary <https://orcid.org/0000-0002-9883-7460>
 Massimo Meneghetti <https://orcid.org/0000-0003-1225-7084>
 Hironao Miyatake <https://orcid.org/0000-0001-7964-9766>
 Mireia Montes <https://orcid.org/0000-0001-7847-0393>
 Priyamvada Natarajan <https://orcid.org/0000-0002-5554-8896>
 Michelle Ntampaka <https://orcid.org/0000-0002-0144-387X>
 Elena Pierpaoli <https://orcid.org/0000-0002-7957-8993>
 Marc Postman <https://orcid.org/0000-0002-9365-7989>
 Jubee Sohn <https://orcid.org/0000-0002-9254-144X>
 David Turner <https://orcid.org/0000-0001-9658-1396>
 Keiichi Umetsu <https://orcid.org/0000-0002-7196-4822>
 Yousuke Utsumi <https://orcid.org/0000-0001-6161-8988>
 Gillian Wilson <https://orcid.org/0000-0002-6572-7089>

References

Akamatsu, H., Fujita, Y., Akahori, T., et al. 2017, *A&A*, **606**, A1
 Alam, S., Albareti, F. D., Allende Prieto, C., et al. 2015, *ApJS*, **219**, 12
 Albrecht, A., Bernstein, G., Cahn, R., et al. 2006, arXiv:astro-ph/0609591
 Allen, S. W., Evrard, A. E., & Mantz, A. B. 2011, *ARA&A*, **49**, 409
 Applegate, D. E., von der Linden, A., Kelly, P. L., et al. 2014, *MNRAS*, **439**, 48
 Astropy Collaboration, Price-Whelan, A. M., Lim, P. L., et al. 2022, *ApJ*, **935**, 167
 Astropy Collaboration, Price-Whelan, A. M., Sipőcz, B. M., et al. 2018, *AJ*, **156**, 123
 Astropy Collaboration, Robitaille, T. P., Tollerud, E. J., et al. 2013, *A&A*, **558**, A33
 Australian National University 2017, SkyMapper First Data Release (DR1), NCI Australia, doi:10.4225/41/593620AD5B574
 Australian National University 2019, SkyMapper Data Release (DR2), NCI Australia, doi:10.25914/5CE60D31CE759
 Bartolini, C., Ignesti, A., Gitti, M., et al. 2022, *ApJ*, **936**, 74
 Benítez, N. 2000, *ApJ*, **536**, 571
 Bertin, E., & Arnouts, S. 1996, *A&AS*, **117**, 393
 Black, W. K., & Evrard, A. 2022, *MNRAS*, **516**, 1170
 Bonjean, V., Aghanim, N., Salomé, P., Douspis, M., & Beelen, A. 2018, *A&A*, **609**, A49
 Bosch, J., AlSayyad, Y., Armstrong, R., et al. 2019, in ASP Conf. Ser. 523, Astronomical Data Analysis Software and Systems XXVII, ed. P. J. Teuben et al. (San Francisco, CA: ASP), 521

Bosch, J., Armstrong, R., Bickerton, S., et al. 2018, *PASJ*, **70**, S5

Bulbul, E., Randall, S. W., Bayliss, M., et al. 2016, *ApJ*, **818**, 131

Chambers, K. C., Magnier, E. A., Metcalfe, N., et al. 2016, arXiv:1612.05560

Child, H. L., Habib, S., Heitmann, K., et al. 2018, *ApJ*, **859**, 55

Chu, A., Durret, F., & Márquez, I. 2021, *A&A*, **649**, A42

Clarke, T. E., Randall, S. W., Sarazin, C. L., Blanton, E. L., & Giacintucci, S. 2013, *ApJ*, **772**, 84

Coe, D., Benítez, N., Sánchez, S. F., et al. 2006, *AJ*, **132**, 926

Cross, N. J. G., Collins, R. S., Mann, R. G., et al. 2012, *A&A*, **548**, A119

Dark Energy Survey Collaboration, Abbott, T., Abdalla, F. B., et al. 2016, *MNRAS*, **460**, 1270

Dehghan, S., Johnston-Hollitt, M., Colless, M., & Miller, R. 2017, *MNRAS*, **468**, 2645

Dey, A., Schlegel, D. J., Lang, D., et al. 2019, *AJ*, **157**, 168

Dietrich, J. P., Böhnert, A., Lombardi, M., Hilbert, S., & Hartlap, J. 2012a, *MNRAS*, **419**, 3547

Dietrich, J. P., Werner, N., Clowe, D., et al. 2012b, *Natur*, **487**, 202

Donahue, M., Ettori, S., Rasia, E., et al. 2016, *ApJ*, **819**, 36

Edwards, L. O. V., & Patton, D. R. 2012, *MNRAS*, **425**, 287

Erdim, M. K., & Hudaverdi, M. 2019, *MNRAS*, **488**, 2917

Fu, S., Dell'Antonio, I., Chary, R.-R., et al. 2022, *ApJ*, **933**, 84

Fu, S., Zhang, Y., Avestruz, C., & Coronel, R. 2024, *MNRAS*, **530**, 2251

Furnell, K. E., Collins, C. A., Kelvin, L. S., et al. 2018, *MNRAS*, **478**, 4952

Gaia Collaboration 2018, Gaia Data Release 2 (Gaia DR2), European Space Agency, doi:10.5270/esa-ycsawu7

Gaia Collaboration, Brown, A. G. A., Vallenari, A., et al. 2018, *A&A*, **616**, A1

Gaia Collaboration, Prusti, T., de Bruijne, J. H. J., et al. 2016, *A&A*, **595**, A1

Gastaldello, F., Ettori, S., Molendi, S., et al. 2003, *A&A*, **411**, 21

Ginsburg, A., Sipőcz, B. M., Brasseur, C. E., et al. 2019, *AJ*, **157**, 98

Girardi, M., Boschin, W., Nonino, M., Innocentini, C., & De Grandi, S. 2022, *A&A*, **658**, A159

Goldovich, N., Dawson, W. A., Wittman, D. M., et al. 2019, *ApJ*, **882**, 69

Gu, L., Akamatsu, H., Shimwell, T. W., et al. 2019, *NatAs*, **3**, 838

Haines, C. P., Busarello, G., Merluzzi, P., et al. 2018, *MNRAS*, **481**, 1055

Harris, C. R., Millman, K. J., van der Walt, S. J., et al. 2020, *Natur*, **585**, 357

Harvey, D., Robertson, A., Massey, R., & McCarthy, I. G. 2019, *MNRAS*, **488**, 1572

Helou, G., Madore, B. F., Schmitz, M., et al. 1991, in *Astrophysics and Space Science Library*, Vol. 171, *Databases & On-line Data in Astronomy*, ed. M. A. Albrecht & D. Egret (Dordrecht: Springer), 89

Herbonnet, R., von der Linden, A., Allen, S. W., et al. 2019, *MNRAS*, **490**, 4889

Hettmansperger, M., Erben, T., Schneider, P., et al. 2005, *A&A*, **442**, 43

Higuchi, Y., Okabe, N., Merluzzi, P., et al. 2020, *MNRAS*, **497**, 52

Hincks, A. D., Radiconi, F., Romero, C., et al. 2022, *MNRAS*, **510**, 3335

Hirata, C., & Seljak, U. 2003, *MNRAS*, **343**, 459

Huang, H.-J., Mandelbaum, R., Freeman, P. E., et al. 2016, *MNRAS*, **463**, 222

Hunter, J. D. 2007, *CSE*, **9**, 90

IRSA 2022, Galactic Dust Reddening and Extinction, NASA IPAC DataSet, IRSA537, doi:10.26131/IRSA537

Irwin, M. J., Lewis, J., Hodgkin, S., et al. 2004, *Proc. SPIE*, **5493**, 411

Ivezić, Ž., Kahn, S. M., Tyson, J. A., et al. 2019, *ApJ*, **873**, 111

Jarvis, M., Bernstein, G., & Jain, B. 2004, *MNRAS*, **352**, 338

Jarvis, M., Sheldon, E., Zuntz, J., et al. 2016, *MNRAS*, **460**, 2245

Jauzac, M., Jullo, E., Kneib, J.-P., et al. 2012, *MNRAS*, **426**, 3369

Jeffrey, N., Gatti, M., Chang, C., et al. 2021, *MNRAS*, **505**, 4626

Joffre, M., Fischer, P., Frieman, J., et al. 2000, *ApJL*, **534**, L131

Jurić, M., Kantor, J., Lim, K. T., et al. 2017, in *ASP Conf. Ser.* 512, *Astronomical Data Analysis Software and Systems XXV*, ed. N. P. F. Lorente, K. Shortridge, & R. Wayth (San Francisco, CA: ASP), 279

Kettula, K., Giordini, S., van Uitert, E., et al. 2015, *MNRAS*, **451**, 1460

Kim, S. Y., Peter, A. H. G., & Wittman, D. 2017, *MNRAS*, **469**, 1414

Knopp, G. P., Henry, J. P., & Briel, U. G. 1996, *ApJ*, **472**, 125

Lakhchaura, K., & Singh, K. P. 2014, *AJ*, **147**, 156

Lakhchaura, K., Singh, K. P., Saikia, D. J., & Hunstead, R. W. 2013, *ApJ*, **767**, 91

Lewis, J. R., Irwin, M., & Bunclark, P. 2010, in *ASP Conf. Ser.* 434, *Astronomical Data Analysis Software and Systems XIX*, ed. Y. Mizumoto, K. I. Morita, & M. Ohishi (San Francisco, CA: ASP), 91

Lin, J., Wagner, J., & Griffiths, R. E. 2023, *MNRAS*, **526**, 2776

Mandelbaum, R., Hirata, C. M., Seljak, U., et al. 2005, *MNRAS*, **361**, 1287

Mandelbaum, R., Lanusse, F., Leauthaud, A., et al. 2018a, *MNRAS*, **481**, 3170

Mandelbaum, R., Miyatake, H., Hamana, T., et al. 2018b, *MNRAS*, **70**, S25

Mann, A. W., & Ebeling, H. 2012, *MNRAS*, **420**, 2120

Massey, R., Harvey, D., Liesenborgs, J., et al. 2018, *MNRAS*, **477**, 669

Maurogordato, S., Sauvageot, J. L., Bourdin, H., et al. 2011, *A&A*, **525**, A79

McCleary, J., dell'Antonio, I., & Huwe, P. 2015, *ApJ*, **805**, 40

McCleary, J., dell'Antonio, I., & von der Linden, A. 2020, *ApJ*, **893**, 8

McClintock, T., Varga, T. N., Gruen, D., et al. 2019, *MNRAS*, **482**, 1352

McMahon, R. 2011, VHS - VISTA Hemisphere Survey, European Southern Observatory (ESO), doi:10.18727/ARCHIVE/57

McMahon, R. G., Banerji, M., Gonzalez, E., et al. 2013, *Msngr*, **154**, 35

Miyatake, H., Battaglia, N., Hilton, M., et al. 2019, *ApJ*, **875**, 63

Monteiro-Oliveira, R., Doubrawa, L., Machado, R. E. G., et al. 2020, *MNRAS*, **495**, 2007

Navarro, J. F., Frenk, C. S., & White, S. D. M. 1997, *ApJ*, **490**, 493

NED 2019, NASA/IPAC Extragalactic Database (NED), IPAC, doi:10.26132/ NED1

Nevalainen, J., Markevitch, M., & Forman, W. 2000, *ApJ*, **536**, 73

Nord, B., Buckley-Geer, E., Lin, H., et al. 2016, *ApJ*, **827**, 51

Obayashi, H., Makishima, K., & Tamura, T. 1998, *PASJ*, **50**, 537

Oguri, M. 2010, *PASJ*, **62**, 1017

Oguri, M., Takada, M., Okabe, N., & Smith, G. P. 2010, *MNRAS*, **405**, 2215

Okabe, N., & Umetsu, K. 2008, *PASJ*, **60**, 345

Onken, C. A., Wolf, C., Bessell, M. S., et al. 2019, *PASA*, **36**, e033

Parekh, V., Laganá, T. F., Thorat, K., et al. 2020, *MNRAS*, **491**, 2605

Piffaretti, R., Arnaud, M., Pratt, G. W., Pointecouteau, E., & Melin, J. B. 2011, *A&A*, **534**, A109

Planck Collaboration, Ade, P. A. R., Aghanim, N., et al. 2014, *A&A*, **571**, A29

Reiprich, T. H., Veronica, A., Pacaud, F., et al. 2021, *A&A*, **647**, A2

Sanders, J. S., Biffi, V., Brüggen, M., et al. 2022, *A&A*, **661**, A36

Sato, K., Kelley, R. L., Takei, Y., et al. 2010, *PASJ*, **62**, 1423

Schirmer, M., Erben, T., Schneider, P., Wolf, C., & Meisenheimer, K. 2004, *A&A*, **420**, 75

Schlafly, E. F., & Finkbeiner, D. P. 2011, *ApJ*, **737**, 103

Schlegel, D. J., Finkbeiner, D. P., & Davis, M. 1998, *ApJ*, **500**, 525

Schneider, P. 1996, *MNRAS*, **283**, 837

Shin, T.-h., Clampitt, J., Jain, B., et al. 2018, *MNRAS*, **475**, 2421

Sifón, C., Hoekstra, H., Cacciato, M., et al. 2015, *A&A*, **575**, A48

Sohn, J., Geller, M. J., Walker, S. A., et al. 2019, *ApJ*, **871**, 129

STScI 2022, Pan-STARRS1 DR1 Catalog, STScI/MAST, doi:10.17909/ 55E7-5X63

The LSST Dark Energy Science Collaboration, Mandelbaum, R., Eifler, T., et al. 2018, arXiv:1809.01669

Umetsu, K. 2020, *A&ARv*, **28**, 7

Umetsu, K., Sereno, M., Tam, S.-I., et al. 2018, *ApJ*, **860**, 104

Virtanen, P., Gommers, R., Oliphant, T. E., et al. 2020, *NatMe*, **17**, 261

von der Linden, A., Allen, M. T., Applegate, D. E., et al. 2014, *MNRAS*, **439**, 2

Wenger, M., Ochsenebein, F., Egret, D., et al. 2000, *A&AS*, **143**, 9

Werner, N., Churazov, E., Finoguenov, A., et al. 2007, *A&A*, **474**, 707

Whelan, B., Veronica, A., Pacaud, F., et al. 2022, *A&A*, **663**, A171

Wolf, C., Onken, C. A., Luvaul, L. C., et al. 2018, *PASA*, **35**, e010

Zhang, Y., Dietrich, J. P., McKay, T. A., Sheldon, E. S., & Nguyen, A. T. Q. 2013, *ApJ*, **773**, 115

Zhou, C., Tong, A., Troxel, M. A., et al. 2023, *MNRAS*, **526**, 323